12 Stable Boundary Layer

The boundary layer can become stably stratified whenever the surface is cooler than the air. This stable boundary layer (SBL) often forms at night over land, where it is known as a nocturnal boundary layer (NBL). It can also form by advection of warmer air over a cooler surface.

The balance between mechanical generation of turbulence and damping by stability varies from case to case, creating stable boundary layers that range from being well mixed to nonturbulent. Sometimes the SBL turbulence is sporadic and patchy, allowing the upper portions of the boundary layer to decouple from surface forcings. As a result of this complexity, the SBL is difficult to describe and model, and some of the concepts presented in this chapter will change with future research.

12.1 Mean Characteristics

12.1.1 Vertical Profiles

Fig 12.1 shows typical profiles of mean variables in the SBL for the case of weak turbulent mixing. The greatest static stability is near the ground, with stability decreasing smoothly toward neutral with height. If stabilities are great enough near the surface to cause temperatures to increase with height, then that portion of the SBL is classified as a *temperature inversion*. In fact, sometimes the whole SBL is loosely called a *nocturnal inversion*.

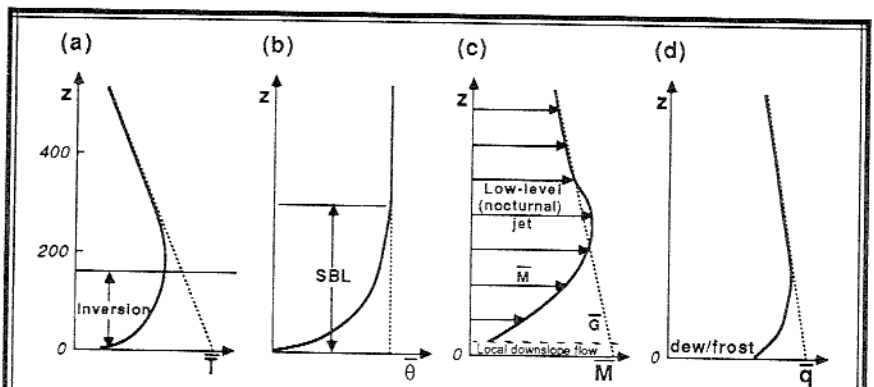

Fig. 12.1 Typical SBL profiles of mean (a) absolute temperature, (b) potential temperature, (c) wind speed, and (d) specific humidity.

In urban areas, a ML can continue throughout the night because of the large heat capacity of buildings and streets, and because of heat released from transportation and space heating. Early evening shallow SBLs in the neighboring rural countryside are not observed in the city. Later at night, when the rural stable layer is deeper than the height of urban buildings, a shallow layer of air within the city can remain well mixed, but it is capped by a stable layer (Godowitch, et al., 1985).

SBL winds can have very complex characteristics. In the lowest 2 to 10 m, cold air will drain down hill. Wind direction in this layer is determined by local topography; wind speed is governed by buoyancy, friction, and entrainment. In flat areas or at the bottom of valleys or topographic depressions, the wind can become calm.

Higher in the SBL synoptic and mesoscale forcings become important. The wind speed can increase with height, reaching a maximum near the top of the stable layer. The layer of peak wind speed is sometimes greater than the geostrophic speed, and is called the ***nocturnal jet.*** Wind directions often ***veer*** (turn clockwise) with height. Above the jet, the wind speed and direction smoothly change to geostrophic. The wind profile is often not in steady-state, and evolves with time during the night.

Humidity is also difficult to classify, because sometimes evaporation from the surface continues at night, while at other locations or times condensation results in dew or frost formation. In cases of reduced turbulence, strong moisture gradients can occur near the surface. The delicate balance between turbulence and stability is apparent in the formation of fog vs. dew, and in the fog processes of dissipation, thickening, or lifting. Fog processes will be discussed in Chapter 13.

Pollutants or other scalar tracers that are emitted into the SBL spread out horizontally in thin layers. This process is called ***fanning*** (see Fig 1.10). Even without tracer emission from a single source at night, the strong wind shears and wind direction changes advect in air of differing tracer concentrations at different altitudes, resulting in a "layer-cake" pattern of tracer concentration (see Fig 12.2). This layered fine-scale vertical structure in aerosols is also apparent in temperature, humidity, and turbulence (Gossard,

et al., 1985). Since there is little vertical mixing, photosensitive constituents already present in the layers of air can chemically react during the night in the absence of solar radiation.

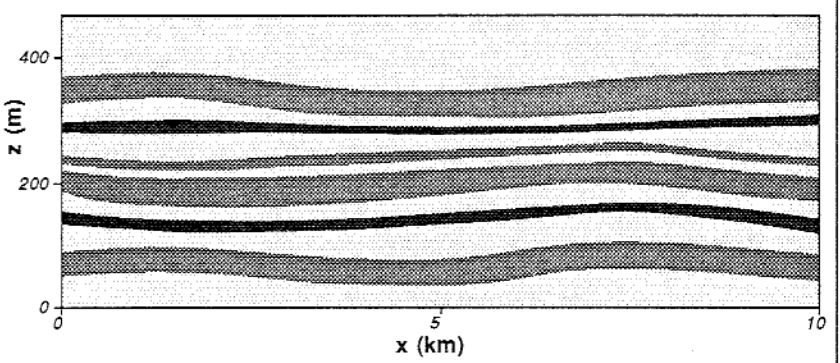

Fig. 12.2 Sketch of the layered aerosol structure often seen by lidar in SBLs. (After Eloranta, personal communication, 1987).

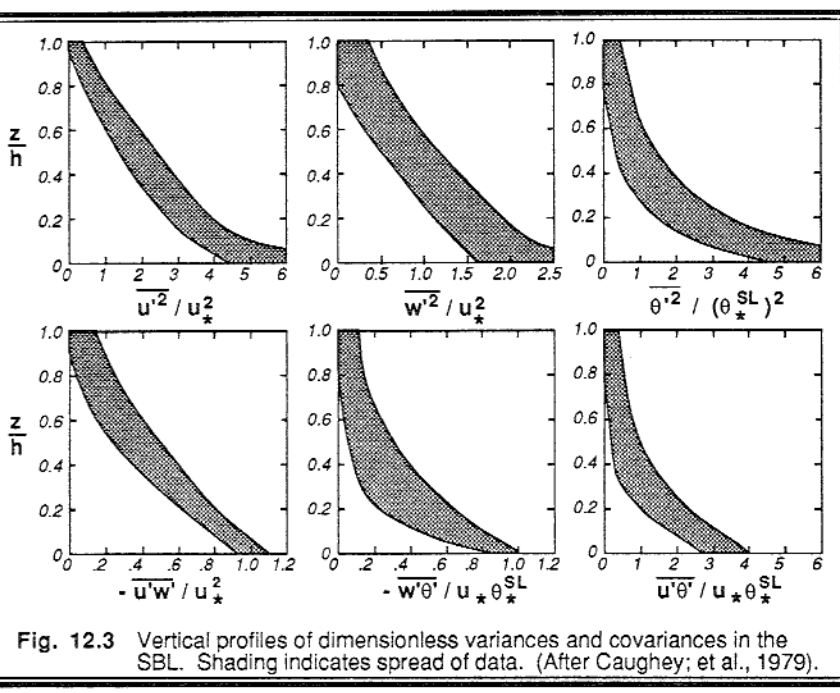

Fig. 12.3 Vertical profiles of dimensionless variances and covariances in the SBL. Shading indicates spread of data. (After Caughey; et al., 1979).

Fig 12.3 shows an idealization of vertical profiles of some turbulent quantities for the weakly turbulent case, based on the previous data from Chapters 3 to 5. Turbulence,when averaged over long times, decreases smoothly with height. At the top of the SBL, the turbulence blends into the residual layer turbulence, or can become nonturbulent. Vertical turbulent motions are suppressed by stability, but buoyant oscillations can occur as ***gravity waves.***

An instantaneous snapshot of turbulence gives a far different picture. Patchy turbulence can occur in thin layers, and turbulent bursting can cause sporadic vertical mixing. Turbulence at height z is governed by local shears and stability at that height rather than by forcings at the surface. For some cases, this results in local ***z-less*** scaling of turbulence, and ***decoupling*** of the flow state from the ground state. Turbulence can be suppressed or enhanced by the passage of gravity waves, can ride up and down hundreds of meters on these waves, and can nonlinearly interact with them.

12.1.2 Bulk Measures of SBL Depth and Strength

Even if turbulence in the SBL is weak, patchy and sporadic, cases can occur where flow-state information is eventually transferred throughout the SBL depth, given a sufficient time interval. Over a long averaging time, these SBLs can act like a single entity, rather than like a group of completely decoupled layers. For the subset of SBL cases ranging from this weakly-coupled one through the strongly-mixed SBL, we can treat the SBL as a single entity with a characteristic bulk strength, depth, and turbulence intensity.

SBL ***strength*** is defined by the near-surface potential-temperature difference:

$$\Delta\overline{\theta}_s = \overline{\theta}_o - \overline{\theta}_s \qquad (12.1.2a)$$

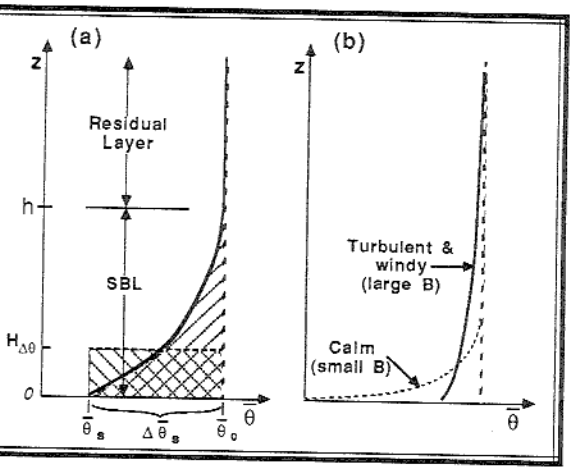

Fig. 12.4 (a) Definitions of SBL strength, $\Delta\overline{\theta}_s$, and depth, h. The integral depth scale, $H_{\Delta\theta}$, is defined such that the shaded area within the rectangle $H_{\Delta\theta} \cdot \Delta\overline{\theta}_s$ equals the area under the potential temperature sounding. (b) Variation of bulk turbulence parameter, B, and profile shape with turbulence intensity.

between the residual layer air, $\overline{\theta}_o$, and the near-surface air, $\overline{\theta}_s$. This is a measure of the amount of cooling that has occurred since SBL formation (i.e., since ***transition***), because the potential temperature of the residual layer is close to the initial near-surface air temperature at transition time (Fig 12.4). Typical magnitudes for SBL strength range from zero at transition to values on the order of 15°C by morning, depending on the turbulence intensity and cloud cover.

The height, h, of the top of the SBL (i.e., the SBL ***depth***) is more difficult to quantify, because in many cases the SBL blends smoothly into the residual layer (RL) aloft without a strong demarcation at its top. Thus, many of the definitions of SBL depth that appeared in the literature are based on relative comparisons of SBL state aloft to near-surface state. For example, h can be defined as the lowest height where:

- $\partial\overline{\theta}/\partial z = 0$ (stable layer top; i.e., the height where the lapse rate is adiabatic)
- $\partial\overline{T}/\partial z = 0$ (inversion top; i.e., the height where the lapse rate is isothermal)
- TKE $= 0$ (top of the turbulent layer, or mixed layer if one exists)
- TKE $= 0.05$ TKE (height where turbulence is 5% of its surface value)
- $\overline{u'w'} = 0$ (top of the stress layer)
- $\overline{u'w'} = 0.05\ \overline{u'w'}_s$ (height where stress is 5% of its surface value)
- $\overline{M}$ is maximum (the nocturnal jet level)
- $\overline{M} = \overline{G}$ (bottom of free atmosphere, where winds are geostrophic)
- sodar returns disappear (top of the layer with temperature fluctuations)

Typical magnitudes for height of the top of the SBL range from near zero at transition time to over 1000 m. Usually, however, SBLs grow to depths of about 100 to 500 m.

Those definitions requiring a gradient or flux to equal zero are extremely difficult to use, because those quantities often approach, but never exactly equal zero. Also, different investigators might use the same criteria with the same data and still select different SBL depths, given errors in the experimental data. It has been difficult to compare SBL models and normalized data, because different investigators have used different depth definitions. Mahrt and Heald (1979) have shown that for some cases, these different definitions are poorly correlated with each other, even for the same SBL.

An alternative measure of the SBL depth is the ***integral depth scale***, H_ξ, where:

$$H_\xi = \frac{\int_z \xi\, dz}{\xi_s} \qquad (12.1.2b)$$

and ξ is any appropriate variable. For example, ξ can be TKE, $\overline{u'w'}$, or it can be $\Delta\overline{\theta}$, where $\Delta\overline{\theta}(z) = \overline{\theta}_o - \overline{\theta}(z)$. This definition for a depth scale can be applied even if there is no sharp demarcation at the SBL top (Fig 12.4). Typical magnitudes for $H_{\Delta\theta}$ range from 0 to about 150 m.

Rearranging (12.1.2b) and substituting $\Delta\theta$ for ξ shows that the ***accumulated cooling*** within the SBL is:

$$\int_0^h \Delta\theta \, dz = \Delta\theta_s \cdot H_{\Delta\theta} \qquad (12.1.2c)$$

A ***bulk turbulence scale***, B, can be defined from the bulk depth scale, which for temperature becomes:

$$B = \frac{H_{\Delta\theta}}{\Delta\overline{\theta}_s} \qquad (12.1.2d)$$

Large values of B correspond to deep SBLs with small surface temperature change, while small values correspond to shallow $H_{\Delta\theta}$ and large surface cooling. Hence, B is a measure of the overall effect of external forcings on the SBL. Typical magnitudes range from 3 m/K for light turbulence through 15 m/K for strong turbulence.

12.1.3 Idealized Models for the Potential Temperature Profile

The wide variety of observed flow states has resulted in a variety of idealized models for the long-time averaged picture of SBLs. No single model works for all situations, so the best model should be chosen on a case-by-case basis.

Stable Mixed Layer. At the one extreme, strong winds, strong turbulence and weak surface cooling can lead to well-mixed layers (Zeman, 1979) that behave as described in Chapter 11.

$$\Delta\overline{\theta}(z) = \begin{cases} 0 & \text{for } z > h \\ \text{constant} & \text{for } z < h \end{cases} \qquad (12.1.3a)$$

Although buoyancy acts like a sink rather than a source, there is enough mechanical mixing by the wind shears to create a mixed layer (Fig 12.5a). This layer can grow in depth by entrainment, although entrainment rates generally decrease during the night as the stability across the entrainment zone increases. For a well-mixed layer, it is easy to show that the integral depth scale equals the actual SBL depth: $h = H_{\Delta\theta}$.

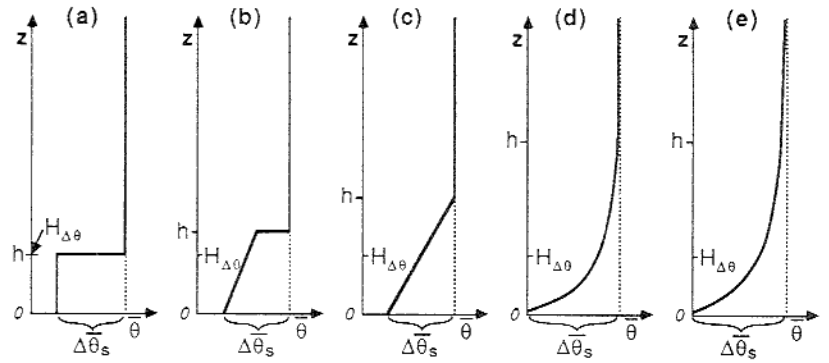

Fig. 12.5 Idealized models of SBL potential temperature profile. (a) well-mixed; (b) linearly-mixed; (c) linear; (d) polynomial; (e) exponential.

The well-mixed SBL can also occur in fog or stratocumulus situations, where strong radiative cooling at cloud top creates convective mixing. For this case, buoyancy is a source of turbulence.

Mixed-Linear. Another idealization allows a potential temperature increase (often linearly) with height, but retains a strong temperature step, $\Delta\bar{\theta}_h$, at the top of the SBL (Fig 12.5b). This can occur with moderately strong winds and turbulence.

$$\Delta\bar{\theta}(z) = \left(1 - \frac{z}{h}\right)\Delta\bar{\theta}_s + \left(\frac{z}{h}\right)\Delta\bar{\theta}_h \qquad (12.1.3b)$$

Above h it is assumed that $\Delta\bar{\theta} = 0$. This not-so-well-mixed layer occurs with slightly weaker mechanical forcings than the previous case. The relationship between top of the SBL and the integral depth scale is $h = 2\,[\Delta\bar{\theta}_s / (\Delta\bar{\theta}_s + \Delta\bar{\theta}_h)]\, H_{\Delta\theta}$.

Linear. A third idealization (Estournel, et al., 1985) describes a linear increase of potential temperature from a finite value near the surface to zero at the top of the SBL (Fig 12.5c).

$$\Delta\bar{\theta}(z) = \left(1 - \frac{z}{h}\right)\Delta\bar{\theta}_s \qquad (12.1.3c)$$

Above h it is again assumed that $\Delta\bar{\theta} = 0$. For this case, $h = 2H_{\Delta\theta}$.

Polynomial. Fourth, the SBL can be described (Yamada, 1979) by a polynomial that passes through the surface value of potential temperature, and has a zero gradient at the top of the SBL (Fig 12.5d).

$$\Delta\bar{\theta}(z) = \left(1 - \frac{z}{h}\right)^{\alpha} \Delta\bar{\theta}_s \qquad (12.1.3d)$$

where parameter α is usually taken as 2 or 3. Above h it is assumed that $\Delta\bar{\theta} = 0$. The relationship between integral depth and SBL top is $h = (1 + \alpha)\, H_{\Delta\theta}$. All four parameterizations above require that h be specified.

Exponential. The last scheme (Stull, 1983; Carlson and Stull, 1986; Surridge and Swanepoel, 1987; Wong, et al., 1987) assumes an exponential potential temperature profile, using $H_{\Delta\theta}$ as the e-folding depth (Fig 12.5e).

$$\Delta\bar{\theta}(z) = \Delta\bar{\theta}_s \, e^{-\frac{z}{H_{\Delta\theta}}} \qquad (12.1.3e)$$

Since there is no well-defined SBL top for this case, we must make an arbitrary assumption. If h is the height where $\Delta\bar{\theta}$ is 5% of it surface value, then $h = 3H_{\Delta\theta}$. Instead, if h is the height where $\Delta\bar{\theta}$ is 2% of it surface value, then $h = 4H_{\Delta\theta}$. This demonstrates the possible magnitudes of h-errors for a profile with no well-defined top.

12.2 Processes

Forcings that act on the SBL include radiation, conduction, turbulence, subsidence and advection. An additional forcing, local terrain slope, will be discussed separately in Section 12.7. It will be shown that none of these forcings can be neglected.

12.2.1 Radiation

Unsaturated conditions. The absence of solar radiation in nocturnal boundary layers allows one to focus on only the longwave radiation budget (i.e., $Q^* = I^*$). Strong radiative cooling of the ground surface occurs at night, with net upward radiative fluxes of about 100 W/m^2 (0.8 K m/s), as already discussed in Chapter 7. In addition, radiation divergence within the air causes small, but significant, cooling in the boundary layer above the ground. This in-situ radiative cooling was neglected for the ML, but can not be neglected in the SBL because many of the other flux terms are small too.

Water vapor is the most important constituent controlling the infrared radiation budget, with carbon dioxide playing a smaller role. In spite of the importance of water vapor, the radiation budget is rather insensitive to the exact amount of moisture present, unless the air becomes saturated and fog or stratocumulus forms.

Typical values of net longwave radiative flux (positive upward) are about 100 W/m^2 in the boundary layer. The radiative flux increases slightly with height, as shown in Fig 12.6a, resulting in flux divergence and radiative cooling at every height. Greater flux divergence often occurs in the lowest tens of meters. The flux divergence and radiative cooling are related by:

$$\left.\frac{\partial \bar{\theta}}{\partial t}\right|_{\text{radiative}} = -\frac{\partial I^*}{\partial z} \qquad (12.2.1a)$$

which is a simplification of (3.5.3f).

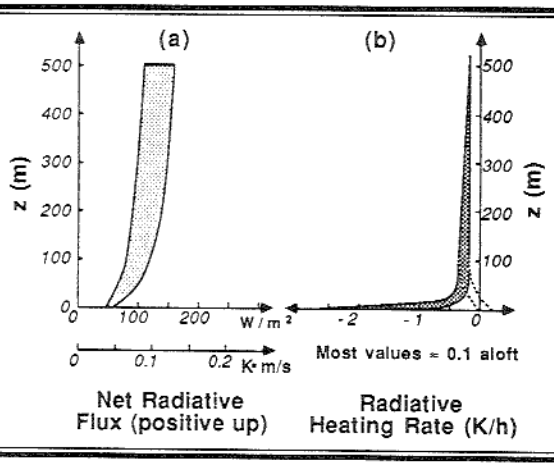

Fig. 12.6 Variation of (a) net radiation within the SBL, and (b) the resulting radiative cooling rate. Some investigators suggest that there is heating, rather than cooling, in the air near the ground (shown dashed in (b)). Garratt and Brost, 1981; Turton and Brown, 1987; Cerni and Parish, 1984; Andre and Mahrt, 1982; Carlson and Stull, 1986; Stull, 1983.

Many studies (Garratt and Brost, 1981; André and Mahrt, 1982; Stull, 1983; Cerni and Parish, 1984; Carlson and Stull, 1986; Turton and Brown, 1987) have indicated a constant cooling rate of 0.1 K/h at heights above 500 m, with cooling rates increasing slowly to about 0.2 K/h at 50 m (see Fig 12.6b). Within a few meters of the ground the cooling rate increases to 1 to 3 K/h in many cases. Temperature inversions near the ground, however, can occasionally lead to radiative heating from the warmer air aloft.

Models. It is beyond the scope of this book to go into the details of radiative transfer models, other than to briefly discuss some of the general approaches (Cerni and Parish, 1984). (1) The ***line-by-line*** approach uses spectral-line information to calculate absorption and emission as a function of wavelength. This is the most accurate method, but is also the most computationally expensive. (2) The ***band*** method uses average absorption and emission over a smaller number of wavelength bands, and is less

expensive and less accurate. (3) The ***flux-emissivity***, or ***graybody***, method assumes that each atmospheric layer can be represented by a single transmissivity or emissivity averaged over all wavelengths. This approach is the least expensive to use, but is sufficiently accurate for many applications. Mahrt (personal communication) notes that any of the three models can give poor results if the vertical resolution near the surface is too coarse.

Using the flux-emissivity method, the net upward longwave flux, I^*, at any height z is described by:

$$I^*(z) = \underset{I}{\int_0^{\varepsilon_{FB}} \sigma_{SB} T^4 d\varepsilon_F} - \underset{II}{\int_0^{\varepsilon_{FT}} \sigma_{SB} T^4 d\varepsilon_F} + \underset{III}{(1 - \varepsilon_{FB}) \sigma_{SB} T_G^4} \quad \underset{IV}{} \qquad (12.2.1b)$$

Term I represents the net longwave flux upward
Term II gives the amount of upward radiation reaching z from all levels below z
Term III gives the amount of downward radiation from all levels above z
Term IV represents the amount of radiation emitted from the surface that is not absorbed by the time it gets to level z.

The flux emissivity, ε_F, is found from tables (e.g., Staley and Jurica, 1970), graphs or other parameterizations (Cerni and Parish, 1984; Chou, 1984), and is a function of the optical thickness, u(z,Z), between the height of interest, z, and any other height Z where the radiation was emitted. The absolute temperature, T, is also evaluated at height Z; and T_G is the surface radiative skin temperature. Emissivities from the bottom of the boundary layer and the (effective) top of the atmosphere are ε_{FB} and ε_{FT}, respectively. Optical thickness is given by:

$$u(z,Z) = \left| \int_{z'=z}^{z'=Z} q \, dz' \right| \qquad (12.2.1c)$$

Equation (12.2.1b) must be solved numerically, using the observed temperature soundings and the parameterizations for flux emissivity (Cerni and Parish, 1984). See Section 13.2 for more discussion on radiation.

The bulk heat flux, Q_R, associated with radiation divergence across the whole SBL is defined as the difference in longwave radiative flux between the bottom and top of the SBL, and is negative when radiative cooling occurs:

$$Q_R = I^*_s - I^*_h \qquad (12.2.1d)$$

12.2.2 Conduction

As in other boundary layers, conduction is small enough to be negligible everywhere except within a few millimeters above the ground. Within these few millimeters, however, the molecular flux dominates over the turbulent flux, and is responsible for the cooling of air in these lowest layers. Above this height, turbulence can transport the colder air upward into the remainder of the SBL. As before, the ***effective turbulent flux*** at ground level, Q_H, is composed mostly of the molecular flux, because the true turbulent flux goes to zero at the surface.

Within these few millimeters, molecular diffusion and conduction control dew and frost formation at night. Dew forms primarily at the tips (i.e., points) of blades of grass, because diffusion of water vapor from the air towards the tip can come from the largest range of angles. Also, the tips can radiate over a large range of angles towards the sky, without experiencing as much return radiation from other objects (like other blades of grass). The reader is directed to any of the cloud microphysics texts for more details of droplet and ice crystal formation.

12.2.3 Turbulence

Turbulence Classification. A variety of types of turbulence can occur in the SBL (Mahrt and Gamage, 1987). In some situations, the SBL is continuously and strongly turbulent over the whole depth of the SBL. In other situations, turbulence might be patchy, weak and intermittent, but when time averaged over a couple hours the average turbulence flux might appear to be acting over the whole SBL depth. Finally, some observations show turbulence aloft that is relatively disconnected with processes at the surface.

In the absence of fog or stratocumulus, turbulence is generated only mechanically in the SBL, usually by wind shears. Wind shear can be created near the ground by friction acting on the ambient flow. It can be generated aloft by variations in the geostrophic wind speed with height. When a low-level jet forms, shears can be enhanced both below and above the nose of the jet. Over sloping terrain, shears can develop at the top of the layer of drainage flow (Mahrt, 1985). Also, shears can be enhanced or reduced at different locations relative to the phase of buoyancy waves. Finally, flow around obstacles such as trees and buildings can generate wake turbulence.

Time scales. Brost and Wyngaard (1978) suggested that a timescale for the effects of turbulence on the whole SBL is approximately:

$$\tau_R = \frac{h}{0.01\, u_*} \qquad (12.2.3a)$$

This scale represents the time it takes for surface information to be communicated across the depth of the SBL via turbulence. Using typical ranges of values for u_* and h for weak

turbulence, we find that τ_R is on the order of 7 to 30 h. Thus, changes in surface forcings might not be felt near the top of the SBL until many hours later if the turbulence is weak.

Compared with the 10 to 15 min time scales for convective ML turbulence, we see that the weakly turbulent SBL is essentially not in equilibrium with its surface forcings (i.e., with surface heat flux or roughness). The SBL is trying to react to surface changes, but is always lagging behind by several hours. Therefore, we can not expect similarity theory to work if our key variables are the surface forcing variables, and we anticipate that statistically robust fluxes and variances might be difficult to measure. Another way to look at it is that since typical mid-latitude nights last about 12 h, the weakly turbulent NBL cannot approach equilibrium before the night ends and the NBL disappears.

Another time scale for motions in the SBL is the inverse of the Brunt-Väisälä frequency, $1/N_{BV}$. This is related to the period of oscillation of a parcel in a statically stable environment, and is discussed in the section on buoyancy waves.

Length Scales. One length scale for turbulence within the SBL is given by:

$$l_B = \frac{\sigma_w}{N_{BV}} \tag{12.2.3b}$$

which indicates the degree of suppression of vertical motions by the static stability. This scale is called the ***buoyancy length scale***, and it can range from a couple hundred meters for weak stratification, to less than a meter for weak turbulence in strong stratification.

Mahrt and Gamage (1987) defined a length scale based on the structure functions for vertical velocity [$D_{ww}(r)$] and potential temperature [$D_{\theta\theta}(r)$], for separation distance r:

$$l_{SB}(r) = \frac{D_{ww}(r)}{(g/\theta_v)\,[\,D_{\theta\theta}(r)\,]^{1/2}} \tag{12.2.3c}$$

For SBLs with strong stability and weak turbulence, this ***structure buoyancy length scale*** is on the order of a meter, while for weak stability and strong turbulence, the scale can be 50 to 100 m. Mahrt and Gamage also used structure functions to study the anisotropy of turbulence, and found that the ratio of vertical to horizontal scales of large turbulent eddies ranged from 0.1 for strong stratification to about 0.5 for weaker stratification.

A ***dissipation length scale*** (Hunt, et al., 1985) can be defined by:

$$l_\varepsilon = 0.4\,\frac{\sigma_w^3}{\varepsilon} \tag{12.2.3d}$$

which typically ranges from 10 to 100 m.

The ***Ozmidov scale*** (Hunt, et al., 1985) is given by:

$$l_O = \left(\frac{\varepsilon}{N_{BV}^3} \right)^{1/2} \qquad (12.2.3e)$$

Typical values range from 10 to 100 m.

The inverse of the wavelength at the peak in the spectrum of $f \cdot S_w(f)$ can also be used to define a length scale (Hunt, et al., 1985). Typical values are 10 to 50 m.

Another length scale, already reviewed in Chapter 9, is the local Obukhov length, L_L (Nieuwstadt, 1984). Typical values range from zero to 50 m; it usually approaches zero as height increases. In the case of strong contiguous turbulence, the Obukhov length based on surface fluxes can be used instead.

A variety of mixing-length scales have be used successfully to model the SBL, because of the absence of large eddies (Estournel and Guedalia, 1987; Lacser and Arya, 1986; and Delage, 1974). For example, Delage's (1974) suggestion was:

$$\frac{1}{l} = \frac{1}{k\,z} + \frac{f_c}{0.0004\,G} + \frac{\beta}{k\,L_L} \qquad (12.2.3f)$$

where β is an empirical parameter. Additional parameterizations are a function of the Richardson number.

Continuous/Contiguous Turbulence. Cooling rates and heat fluxes for a couple of cases are shown in Fig 12.7. Unlike the corresponding radiation figure, the variation of heat flux and cooling rate from case to case varies so widely that it is useless to show the whole possible range on one figure. Given a turbulent heat flux into the bottom of the

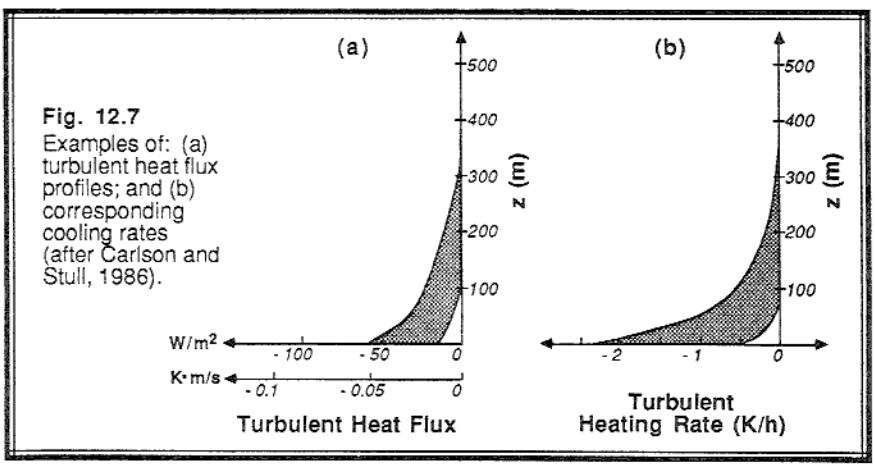

Fig. 12.7 Examples of: (a) turbulent heat flux profiles; and (b) corresponding cooling rates (after Carlson and Stull, 1986).

SBL, and no turbulence at the top, the bulk turbulent heat flux is equal to the surface flux, Q_H.

Similarity theory is useful for the contiguously turbulent SBL, where surface forcings can be used as the key scaling variables. Such parameterizations were described in Chapter 9, and were used to scale the variables in Fig 12.3. Also, K-theory, higher-order closure models, and transilient theory have also been successfully applied to the SBL.

For the continuously and contiguously turbulent situation that is in equilibrium with the surface, it is reasonable to use the bulk measures of turbulence described earlier. We expect greater turbulence to occur in stronger winds and over rougher ground. However, weaker turbulence is anticipated during cases of strong cooling at the surface. These influences can be incorporated into a parameterization (Stull, 1983) for the bulk turbulence:

$$B = \frac{\left(\left| f_c G \right| Z_s \right)^{3/2}}{(- g Q_H)} \qquad (12.2.3g)$$

where Z_s is a measure of the surface roughness averaged over many kilometers upwind. The roughness factor, Z_s, is not like a roughness length, but has values on the order of 2 to 10 km. This roughness factor must be determined aerodynamically for each wind direction at each site based on observed SBL development, because no direct description for it has appeared in the literature.

Instead of using wind speed directly in the above parameterization the pressure gradient forcing $f_c G$ is used because it drives the winds (Estournel and Guedalia, 1985). Note that the definition of G includes a factor of $1 / f_c$, thus making the product $f_c G$ independent of f_c, as required for these schemes to work in tropical regions. The variation of B with geostrophic speed and direction for Wangara is shown in Fig 12.8.

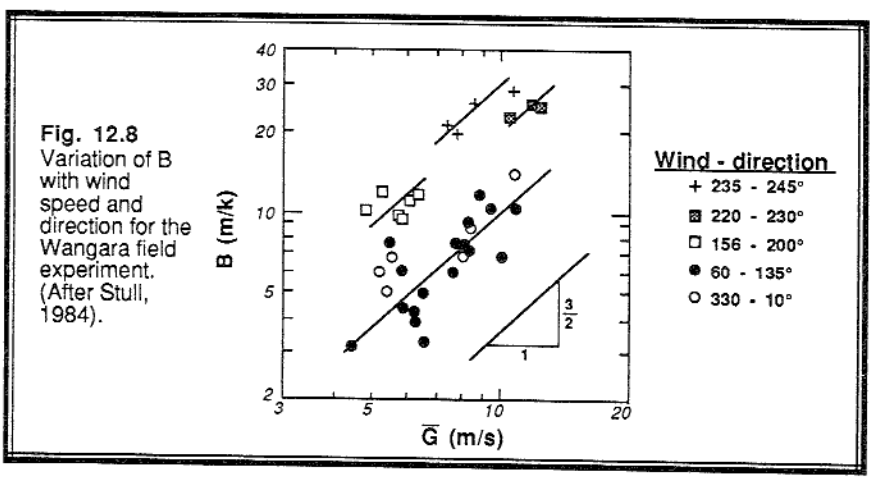

Fig. 12.8 Variation of B with wind speed and direction for the Wangara field experiment. (After Stull, 1984).

Patchy Turbulence in Equilibrium with the Surface. We have already seen in Fig 12.3 an example of time-averaged turbulence variables, during which the SBL might not have been turbulent at all times or at all heights during the averaging period. Nevertheless, we can often utilize the continuous/contiguous turbulence parameterizations described above to model this time-averaged SBL.

One phenomenon sometimes seen in the SBL is an occasional bursting of turbulence. It is speculated that in nonturbulent SBLs, wind shears can increase because of the dynamic forcings and the lack of mixing. Eventually, the shears are great enough to trigger turbulence (i.e., the Richardson number is low enough). This burst of turbulence causes vertical mixing of both heat and momentum, causing shears to decrease and the Richardson number to increase. Eventually, the shears are too weak to continue to support turbulence, and turbulence ceases. During the resulting quiescent period, shears can again build to the point of another turbulent burst. Such a scenario can also occur with discontinuous turbulence, described next.

Discontinuous Turbulence. In situations where turbulence aloft is disconnected with the surface, it has been shown in Chapter 9 that local ***z-less*** similarity scaling can be used (Wyngaard, 1973; Nieuwstadt, 1984). Turbulence variables are consistent with, and scale to, each other, but do not scale with surface forcings. In order to use this approach, one must first measure a subset of the turbulence variables aloft, against which the remaining variables can be related. Although this is a useful diagnostic tool to relate variables within the turbulent layer, it precludes forecasts or parameterizations. The assumption of constant Richardson number is often made with z-less scaling, although as shown below the Richardson number is rarely constant with time or location.

The Richardson number is one of the indicators for the location of turbulence within the SBL. Fig 12.9 (André and Mahrt, 1982) shows the potential temperature and wind profiles for one case study, and also shows the corresponding vertical profile of Richardson number. Regions of Richardson number less than 0.5 are shaded, and

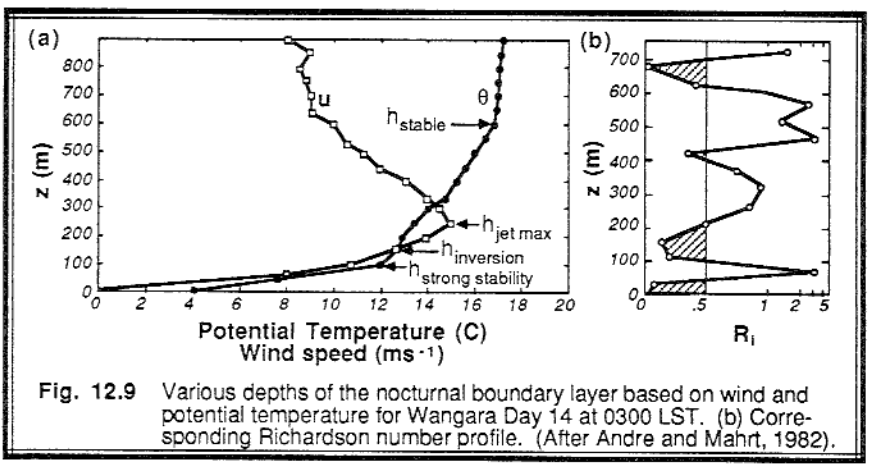

Fig. 12.9 Various depths of the nocturnal boundary layer based on wind and potential temperature for Wangara Day 14 at 0300 LST. (b) Corresponding Richardson number profile. (After Andre and Mahrt, 1982).

indicate layers where turbulence is likely. During the night, these turbulent layers can form and dissipate, and reform at other heights. Mahrt, et al. (1979) found that the Richardson number is large at altitudes corresponding to the LLJ maximum, but they found smaller Richardson numbers and more intense turbulence just above the jet where shears are stronger and static stability is weak.

Forecasting the Richardson number for the SBL can be tenuous because of its sensitivity to relatively small changes in potential temperature and wind profile gradient (see Fig 12.10, for a different case, after Gossard and Frisch, 1987). Also, coarse measurement of the bulk Richardson number across a thick layer might yield a large value (i.e., nonturbulent), while measurements made at higher resolution over the same region might indicate the possibility of thin layers of low Richardson number (i.e., turbulent).

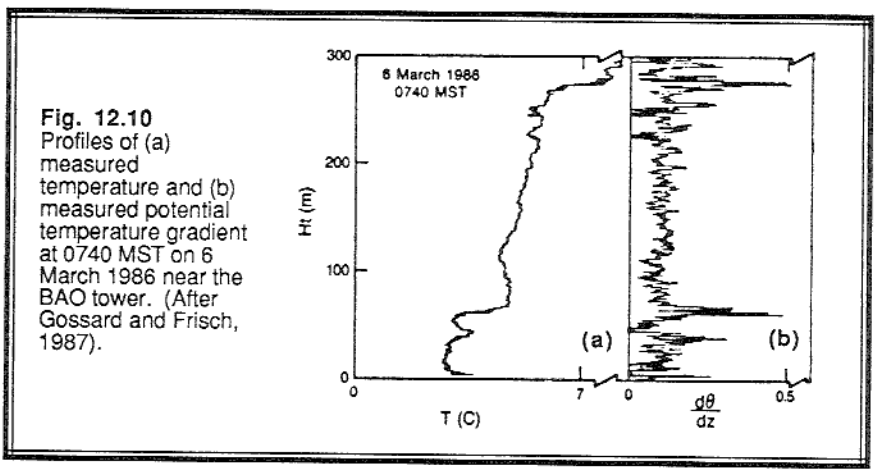

Fig. 12.10 Profiles of (a) measured temperature and (b) measured potential temperature gradient at 0740 MST on 6 March 1986 near the BAO tower. (After Gossard and Frisch, 1987).

12.2.4 Subsidence and Advection

Subsidence. The fair weather conditions associated with clear skies and strong nocturnal radiative cooling are also those associated with anticyclones, divergence and subsidence. During such conditions, Carlson and Stull (1986) found vertical velocity values of -0.1 to -0.5 m/s near the top of the SBL. Subsidence causes warming by bringing down warmer air from aloft. The local warming rate is thus simply the product of the subsidence and the local vertical gradient of potential temperature:

$$\left.\frac{\partial \bar{\theta}}{\partial t}\right|_{\text{subsidence}} = -\,w\,\frac{\partial \bar{\theta}}{\partial z} \qquad (12.2.4a)$$

Typical heating rates due to subsidence are shown in Fig 12.11. These heating rates are as large as, and sometimes larger than, the radiative and turbulent cooling rates. Thus, neglect of subsidence in the SBL heat budget is not recommended.

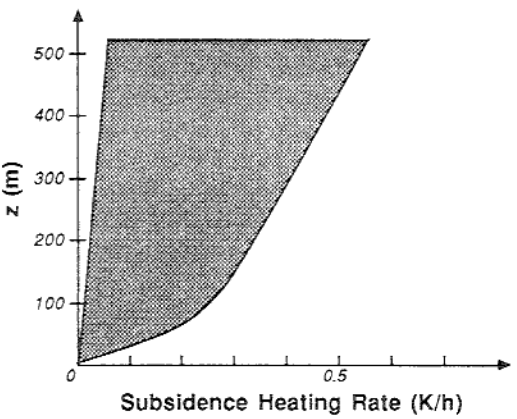

Fig. 12.11
Range of heating rates associated with subsidence in the SBL (after Carlson and Stull, 1986).

Another way to look at the effects of subsidence is to recognize that the associated divergence, Div, is removing some of the chilled air from the SBL. Using $\Delta\theta_s \cdot H_{\Delta\theta}$ as a measure of the accumulated cold air within the SBL, the effective bulk heat flux into the whole SBL, Q_w, that would cause heating equal to the amount of cold air lost is:

$$Q_w = \text{Div} \cdot \Delta\theta_s H_{\Delta\theta} \qquad (12.2.4b)$$

Typical magnitudes of this flux are 0.01 K m/s.

It is possible to have BL cooling and SBL formation in regions of convergence, where warm air advection over a colder surface can provide the cooling in the absence of radiative cooling. Convergence sweeps together the surrounding cold air to make a deeper and/or colder SBL than would have otherwise occurred via local processes. The equations (12.2.4a & b) can be used, recognizing that Div is negative and w is positive.

Advection. Often the largest term in the heat budget of the SBL is advection, yet it is the one least often considered or measured. Schaller and Wichmann (1985) and Carlson and Stull (1986) have demonstrated that advective heating rates can easily range between ± 2 K/h, where the heating rate is given by:

$$\left.\frac{\partial \overline{\theta}}{\partial t}\right|_{\text{advection}} = - \overline{U}_j \frac{\partial \overline{\theta}}{\partial x_j} \qquad (12.2.4c)$$

for j = 1 and 2.

Furthermore, advection can be a strong heat source in one part of the SBL, and a heat sink in other parts. The effective bulk heat flux, Q_A, associated with horizontal advection into the whole SBL is:

$$Q_A = -\int_0^h \overline{U_j} \frac{\partial \overline{\theta}}{\partial x_j} \, dz \qquad (12.2.4d)$$

for j = 1 and 2.

Traditional means of measuring advection must be used with care, because advection will tend to follow isentropic surface, except where the surfaces touch the ground or where there is mixing in the vertical. The synoptic rawinsonde network might not offer sufficient resolution in the vertical nor horizontal to adequately measure the advection at night.

There is no simple way to parameterize this term. It must be calculated directly using a 3-D (mesoscale) forecast model, or it must be measured directly.

12.3 Evolution

12.3.1 Bulk Growth

The combined effects of turbulence, radiation, subsidence and advection cause the SBL to evolve as sketched in Fig 12.12. Shortly after surface cooling starts (e.g., evening), a shallow weak SBL forms, leaving a deep residual layer above it. Gradually, the SBL becomes deeper by the cooling of the lower residual layer. The strength also increases until such time as the surface cooling stops (e.g., morning). The example shown in Fig 12.12 corresponds to one of relatively weak contiguous turbulence.

The evolution of accumulated cooling, $\Delta\theta_s \, H_{\Delta\theta}$, within the continuously/contiguously turbulent SBL is given by a heat balance of all the forcings:

$$-\frac{\partial (\Delta\theta_s \cdot H_{\Delta\theta})}{\partial t} = Q_H + Q_R + Q_w + Q_A = Q_T \qquad (12.3.1a)$$

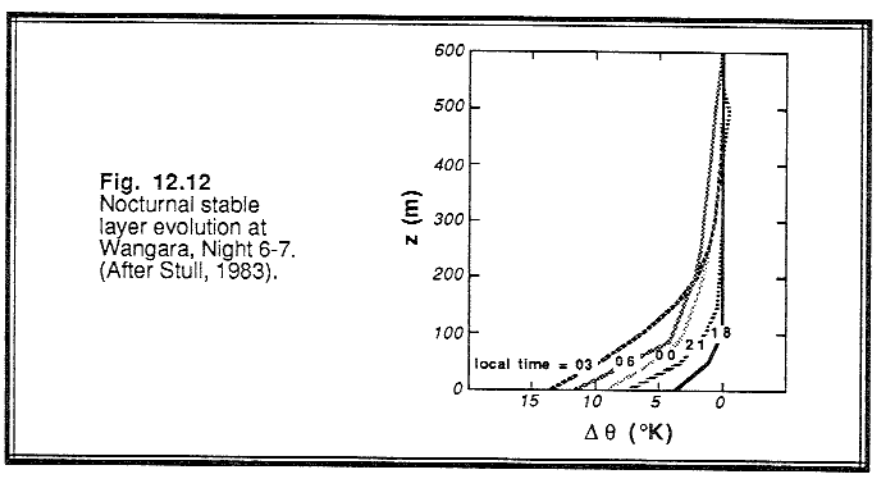

Fig. 12.12 Nocturnal stable layer evolution at Wangara, Night 6-7. (After Stull, 1983).

where Q_T , the total (net) heat flux acting on the bulk SBL, is negative. If Q_T were positive, then there would be net heating causing the SBL to be eliminated.

During most nights Q_T varies significantly with time, requiring (12.3.1) to be integrated numerically. For the special case of constant Q_T, we can employ the definition for bulk turbulence together with (12.3a) to analytically solve for the integral depth and strength of the SBL:

$$H_{\Delta\theta} = \left(- Q_T \; t \; B \right)^{1/2} \tag{12.3.1b}$$

$$\Delta\theta_s = \left(\frac{- Q_T \; t}{B} \right)^{1/2} \tag{12.3.1c}$$

These equations show that the depth and strength increase with the square root of time, as sketched in Fig 12.13. They also show that a more-turbulent SBL (i.e., one with larger B) will be deeper and have less surface cooling than a less-turbulent SBL. The square-root of time growth has been observed by Brunt (1939), Brost and Wyngaard (1978), Stull (1983a,b), Brook, 1985), and Surridge and Swanepoel (1987).

With forecasts of $\Delta\theta_s$ and $H_{\Delta\theta}$, the profile models of Section 12.1.3 can be used to forecast the shape of the potential temperature profile as it evolves throughout the night.

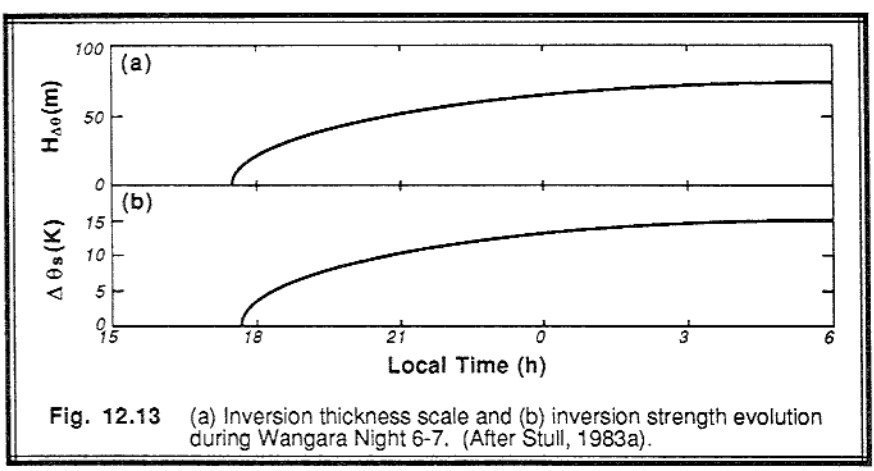

Fig. 12.13 (a) Inversion thickness scale and (b) inversion strength evolution during Wangara Night 6-7. (After Stull, 1983a).

12.3.2 Example

Problem. Given a clear night with brisk geostrophic winds (G = 10 m/s) and strong bulk cooling (Q_T = -0.03 K m/s) at a location where $f_c = 10^{-4}$ s^{-1} and Z_s = 4 km, find the bulk depth and strength of the SBL after 6 h. Also plot the resulting potential temperature profiles for the mixed, linear, and exponential models.

Solution. First, find the bulk turbulence parameter, B:

$$B = \frac{\left(\left| f_c \overline{G} \right| Z_s \right)^{3/2}}{-Q_T\, g} = \frac{[\,(10^{-4})\,(10)\,(4000)\,]^{3/2}}{(0.03)\,(9.8)} = 27.2 \text{ m/K}$$

Next, use B to find $H_{\Delta\theta}$ and $\Delta\theta_S$ at t = 6 h:

$$H_{\Delta\theta} = \left(-Q_T\, t\, B \right)^{1/2} = [\,(0.03)\,(6)\,(3600)\,(27.2)\,]^{1/2} = 132.8 \text{ m}$$

$$\Delta\theta_s = \left(-Q_T\, t / B \right)^{1/2} = [\,(0.03)\,(6)\,(3600) / (27.2)\,]^{1/2} = 4.88 \text{ K}$$

Plots of the profiles are shown in Fig 12.14.

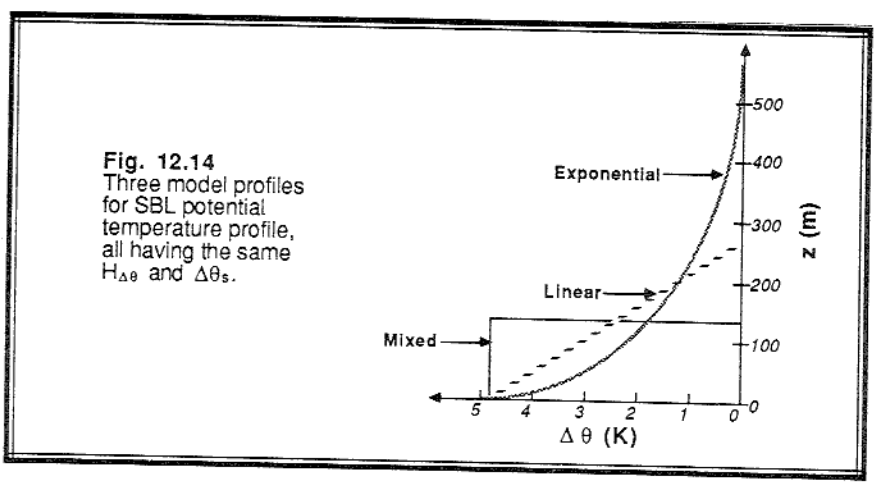

Fig. 12.14 Three model profiles for SBL potential temperature profile, all having the same $H_{\Delta\theta}$ and $\Delta\theta_s$.

Discussion. For this case of strong turbulence, the linear and exponential models are not significantly different. However, all three models give different SBL heights: h = 133 m for the well-mixed model, h = 266 m for the linear model, and h = 398 to 531 m for the exponential model. In spite of the fact that h is poorly defined (and probably should not be used), the bulk depth scale, $H_{\Delta\theta}$, is well defined for all profile shapes.

12.4 Other Depth Models

In some of the earlier research on SBLs, it was hoped that a ***diagnostic equation*** could be found for an equilibrium SBL depth. Later, when the time evolution was

understood better, ***rate equations*** were devised to allow the SBL depth to slowly approach an equilibrium depth. Neither of these approaches yielded the best results, and are only briefly reviewed here.

12.4.1 Diagnostic Models

The following models, sans empirical constants, have been proposed at various times for ***equilibrium SBL depths***, h_{eq}: u_*/f_c, $u_*^2/(f_c G \sin \alpha_{GM})$, $[\, u_* L / |f_c| \,]^{1/2}$, L, G/N_{BV}, $h_{tropopause}$, $G^2 \theta / (g \Delta\theta_s)$, and combinations of these, where α_{GM} is the angle between the geostrophic and surface winds. The last model listed above is based on the assumption that the bulk Richardson number for the whole SBL is constant. None of these diagnostic models were found to be satisfactory, because the SBL is rarely in equilibrium. It evolves with time as cold air is accumulated and as forcings change.

12.4.2 Rate Equations

After diagnostic models were found to be unsatisfactory, an improvement was suggested where the actual depth tends to adjust toward an equilibrium depth, with a response time of τ_R. As a result, the so-called rate equations were born:

$$\frac{dh}{dt} = \frac{h_e - h}{\tau} \qquad (12.4.2)$$

For constant h_{eq}, the equation above describes an exponential approach of h toward h_{eq}, with an e-folding time of τ_R.

Over ten versions of this rate equation are in the literature. Although most are better than the diagnostic approach, they still have some drawbacks. Part of the problem is the assumption that there exists some appropriate equilibrium depth, h_{eq}. Many of the same models of equilibrium depth described in the diagnostic section are also used in the rate equations. A variety of models for response time have been proposed, including: h/u_*, h/G, h/M, $1/f_c$, and $\Delta\theta_s/(d\theta_s/dt)$.

12.4.3 Other Prognostic Models

A few other approaches are suggested in the literature, some of which are of the form: $dh/dt \propto u_* L / h$. Although this yields the appropriate square-root time dependence, it is not a function of the accumulated cooling. This scheme also has difficulties.

Surridge and Swanepoel (1987) found that the square-root time dependence occurs on many occasions at many sites, but not at all sites. For some of the sites, the SBL depth and strength approach equilibrium values with an error-function time dependency:

$$H = H_{eq}\ \mathrm{erf}\left(\frac{t}{\tau_R}\right) \tag{12.4.3a}$$

$$\Delta\theta_s = \Delta\theta_{seq}\ \mathrm{erf}\left(\frac{t}{\tau_R}\right) \tag{12.4.3b}$$

where the response time, τ_R, is on the order of 1 to 2 h for the cases studied. An exponential approach to equilibrium, such as predicted using the rate equations, would have probably worked as well. Their observations of equilibrium values for strength and depth ($\Delta\theta_{seq}$ and H_{eq}, respectively) suggest that radiative cooling must be balanced by other processes such as advection or subsidence for these situations.

12.5 Low-Level (Nocturnal) Jet

12.5.1 Characteristics

As described in Chapter 1, the low-level jet (LLJ) is a thin stream of fast moving air, with maximum wind speeds of 10 to 20 m/s usually located 100 to 300 m above the ground. Peak speeds up to 30 m/s have been reported, and altitudes of the peak were occasionally as high as 900 m above ground. The LLJ can have a width of hundreds of kilometers and a length of a thousand kilometers, making it more like a sheet than a narrow ribbon, in some cases.

The LLJ has been observed in Europe (Sladkovic and Kanter, 1977; Kraus, et al., 1985), Africa (Anderson, 1976; Hart, et al., 1978), North and South America (Blackadar, 1957; Bonner, 1968; Lettau, 1967), and Australia (Malcher and Kraus, 1983;

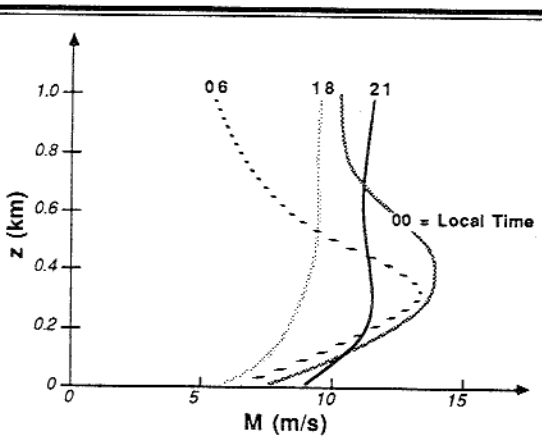

Fig. 12.15 Nocturnal jet evolution during night 13-14 of Wangara. (After Malcher and Kraus, 1983.)

Brook, 1985; Garratt, 1985). In many cases, the LLJ forms during the night and reaches its peak during the predawn hours (Figs 12.15 and 12.16). These LLJs are often called ***nocturnal jets***. Examples include:

- Koorin nocturnal jet (Australia)
- Great Plains nocturnal jet (USA)

In other cases, the jet forms during the daytime:

- Paracas LLJ (Peru)
- Southerly Buster LLJ (East-Australia)

Chile's Atacama boundary layer wind peaks twice, once from the southwest during the afternoon, and then from the northeast at night (Lettau, personal communication). The East African (Somali) jet lasts day and night for many days.

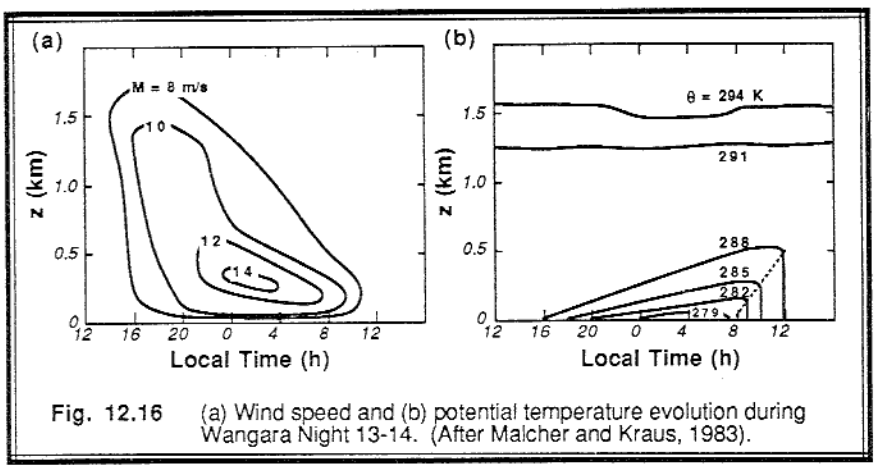

Fig. 12.16 (a) Wind speed and (b) potential temperature evolution during Wangara Night 13-14. (After Malcher and Kraus, 1983).

Different investigators have used different criteria for identifying LLJs. Some have required wind speeds greater than a specific speed (e.g.,12, 16, or 20 m/s) below a specified height (e.g., 1000, 1500, or 2500 m), while others require the speed to be supergeostrophic (Bonner, 1968; Brook, 1985). We will pragmatically define the LLJ as occurring whenever there is a relative wind speed maximum that is more than 2 m/s faster than wind speeds above it within the lowest 1500 m of the atmosphere.

Investigations have shown that there are many possible causes for the LLJ (Kraus, et al., 1985), including:

- synoptic-scale baroclinicity associated with weather patterns
- baroclinicity associated with sloping terrain
- fronts
- advective accelerations
- splitting, ducting and confluence around mountain barriers
- land and sea breezes
- mountain and valley winds
- inertial oscillations

In some situations, more than one of the above factors contribute to jet formation (Garratt, 1985). Thus, there are many different types of LLJs with different characteristics. The first three factors listed above can generate LLJs with subgeostrophic wind speeds. The others can create supergeostrophic winds.

LLJs are not rare phenomena. Brook reports nocturnal jets on 19% of the winter nights in parts of Australia, with peak speeds reached between midnight and 0500 local time. Bonner (1968) observed North American LLJs occurring most frequently in the central plains, particularly in the Kansas and Oklahoma region, where 30% of all rawinsonde soundings had LLJs. Many of these were associated with southerly or southwesterly wind components, and the majority occurred in the late night or early morning. A distinct jet core was observed from Texas to Minnesota. The Somali jet lasts many days, and reoccurs almost every year with the Indian monsoon.

In the following sections two of the LLJ forcings will be examined in detail: baroclinicity over sloping terrain, and the inertial oscillation.

12.5.2 Baroclinicity Over Sloping Terrain

Horizontal temperature gradients cause changes of the geostrophic wind with height, as given by the approximate ***thermal wind*** relationship (Holton, 1972):

$$\frac{\partial U_g}{\partial z} = - \frac{g}{f_c T} \frac{\partial T}{\partial y} \qquad (12.5.2a)$$

$$\frac{\partial V_g}{\partial z} = + \frac{g}{f_c T} \frac{\partial T}{\partial x} \qquad (12.5.2b)$$

For example, given a southerly geostrophic wind at the surface (i.e., V_g is positive), V_g will decrease with height if the air is warmer to the west in the northern hemisphere (Figs 12.17a & b).

If the actual wind is geostrophic everywhere except near the ground (where friction reduces it below geostrophic), then we see in Fig 12.17b that a LLJ is formed given the same situation of southerly geostrophic wind. This is an example of a subgeostrophic LLJ that can occur day or night, although it is less likely to occur during the day because vigorous mixing in the ML would tend to mix the fast LLJ air with the slower air at adjacent levels, leaving a well-mixed wind profile.

The thermal wind associated with baroclinicity can be caused by a variety of forcings, including synoptic-scale temperature gradients, mesoscale land-sea temperature gradients, and gradients across fronts. In regions such as the central USA, ***sloping terrain*** can also generate horizontal temperature gradients that change sign with the diurnal cycle (Lettau, 1967; Holton, 1968). This can lead to a diurnal oscillation in the strength of the LLJ, as shown below.

The scenario of Fig 12.17a corresponds to a late afternoon situation where the ground has been warmed by the sun, and where the temperature decreases adiabatically with height within a deep ML. In any plane at constant height above sea level, the higher terrain in the west causes the temperature there to be warmer than the temperature in the east. This creates the horizontal temperature gradient of the previous example, and causes negative geostrophic wind gradients at all heights within the ML (indicated by the thermal wind vectors labeled T.W. in Fig 12.17a).

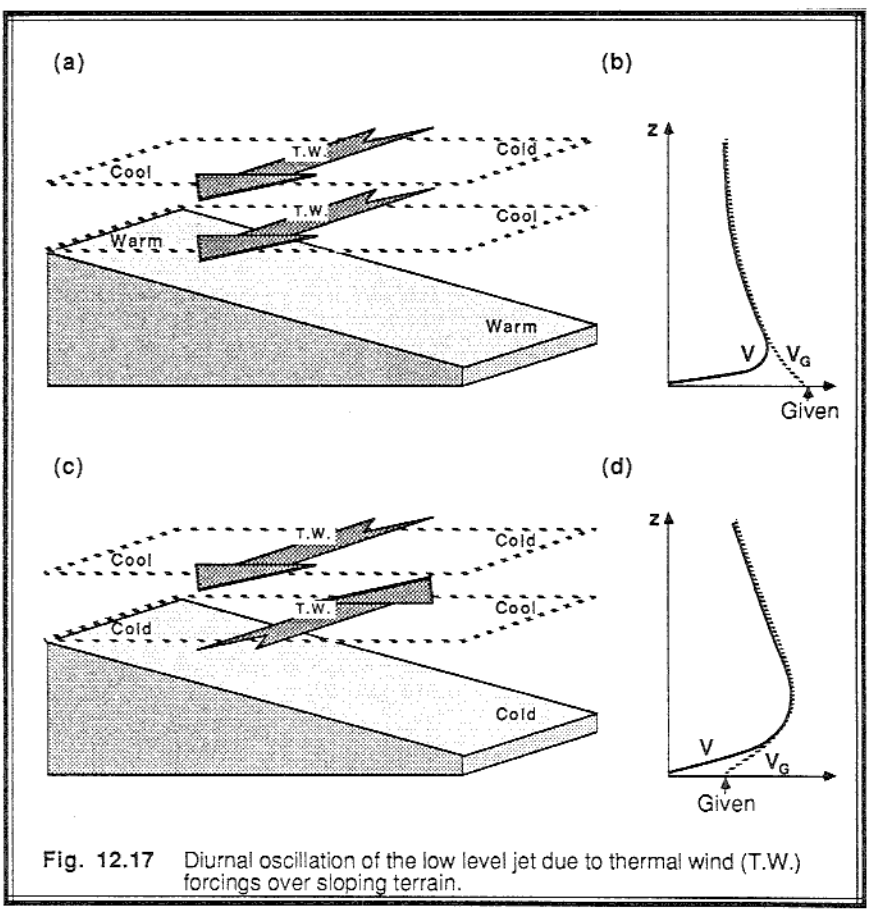

Fig. 12.17 Diurnal oscillation of the low level jet due to thermal wind (T.W.) forcings over sloping terrain.

At night, the ground cools the adjacent air, but not the air higher in the residual layer. This reverses the thermal wind at low altitudes in the SBL, but leaves the thermal wind unchanged higher in the residual layer (Fig 12.17c). The resulting geostrophic wind has a peak at low levels (Fig 12.17d), assuming a southerly surface geostrophic wind. The actual wind has an even more predominant jet, resulting from drag at the surface (Fig 12.17d).

The southerly geostrophic winds often occur in the warm sectors of approaching cyclones in the central USA. These sectors are also sometimes conditionally unstable. Raymond (1978) and Uccellini and Johnson (1979) have shown that thunderstorms can be triggered by LLJs in these situations.

12.5.3 Inertial Oscillation

During the daytime, winds in the ML are subgeostrophic because of strong frictional drag at the ground. At sunset when ML turbulence ceases, pressure gradients tend to accelerate the winds back toward geostrophic. However, the Coriolis force induces an ***inertial oscillation*** in the wind, causing it to become supergeostrophic later at night (Blackadar, 1957). Details of this oscillation are now discussed.

The starting point in this analysis are momentum equations (3.5.3c & d) for the boundary layer. For simplicity, choose a coordinate system such that $V_g = 0$, and abbreviate the Reynolds stress divergence (friction) terms by $\partial\overline{u'w'}/\partial z \equiv f_c \cdot F_u$, and $\partial\overline{v'w'}/\partial z \equiv f_c \cdot F_v$, where F_u and F_v have units of velocity. The equations become:

$$\frac{d\overline{U}}{dt} = +f_c\,\overline{V} \qquad - f_c F_u \tag{12.5.3a}$$

$$\frac{d\overline{V}}{dt} = f_c(\overline{U_g} - \overline{U}) - f_c F_v \tag{12.5.3b}$$

Initially, the winds are subgeostrophic, so we must first determine the daytime ML winds to be used as initial conditions for the nocturnal case. Assuming steady state during the day, the above equations can be easily solved for the winds:

$$\overline{U}_{day} = \overline{U_g} - F_{v\,day}$$

$$\overline{V}_{day} = F_{u\,day} \tag{12.5.3c}$$

In this form, we see that F_u and F_v represent the departure of the winds from geostrophic (i.e., the ***geostrophic departure***).

Next, assume that friction suddenly disappears above the surface layer at sunset, and that friction remains zero throughout the night. The nocturnal winds are expected to evolve with time, so we cannot assume steady state. Combine (12.5.3 a & b) into one equation by taking the time derivative of the first equation, and then substituting in the second equation:

$$\frac{d^2 \overline{U}}{dt^2} = -f_c (\overline{U} - \overline{U_g})$$

The solution will be of the form:

$$\overline{U} - \overline{U_g} = A \sin(f_c t) + B \cos(f_c t)$$

The parameters A and B are then determined from the initial conditions (12.5 3c), yielding $A = F_{u\,day}$ and $B = -F_{v\,day}$. The final result is then:

$$\overline{U}_{night} = \overline{U_g} + F_{u\,day} \cdot \sin(f_c t) - F_{v\,day} \cdot \cos(f_c t)$$

$$\overline{V}_{night} = F_{u\,day} \cdot \cos(f_c t) + F_{v\,day} \cdot \sin(f_c t) \qquad (12.5.3d)$$

We see that the winds oscillate about the geostrophic value, but never converge to the geostrophic value in this idealized scenario. The period of oscillation, called the ***inertial period***, is $2\pi/f_c$. At midlatitudes, the inertial period is about 17 h. The magnitude of the oscillation at night depends on the amount of geostrophic departure at the end of the day. Typical geostrophic departures are on the order of 2 to 5 m/s at the end of the day, leading to nocturnal jet maxima that can be 2 to 5 m/s faster than geostrophic (Garratt, 1985; and Kraus, et al., 1985).

12.5.4 Example

Problem. Frictional drag during the day results in geostrophic departures of $F_u = F_v = 3$ m/s at sunset. Calculate and plot the resulting nocturnal winds for every hour over a full inertial period. Also determine the time of occurrence and maximum speed of the nocturnal jet. Assume $f_c = 10^{-4}\ s^{-1}$, $U_g = 10$ m/s, and $V_g = 0$.

Solution. Solving (12.5.3d) using the conditions above gives the winds listed in the Table 12-1. These are plotted as a hodograph in Fig 12.18. We see that the wind vectors describe a circle about the geostrophic wind, with a radius of 4.24 m/s. A maximum wind speed of 14.24 m/s is reached about 6.5 h after sunset. In fact, the wind speeds are supergeostrophic for about a 9 h period.

Discussion. Initially, the winds are subgeostrophic and cross the isobars toward low pressure, as expected with friction. Shortly after sunset, the winds continue to turn toward low pressure (Mahrt, 1981). However, between 7 and 15 h after sunset the winds cross the isobars toward high pressure during a portion of the inertial oscillation. Such ageostrophic winds can lead to convergence regions that can trigger thunderstorms.

Also, midlatitude nights last only 8 to 16 h, depending on the season and latitude. Thus, the full cycle of the oscillation might not be realized before daytime mixing destroys the nocturnal jet.

Table 12-1. Example of an inertial oscillation.

t (h)	U - U_g (m/s)	V_g (m/s)	t (h)	U - U_g (m/s)	V_g (m/s)
0	-3.00	3.00	10	1.36	-4.02
1	-1.75	3.86	11	-0.14	-4.24
2	-0.28	4.23	12	-1.62	-3.92
3	1.23	4.06	13	-2.90	-3.10
4	2.58	3.37	14	-3.81	-1.88
5	3.60	2.24	15	-4.22	-0.41
6	4.16	0.83	16	-4.10	1.10
7	4.19	-0.69	17	-3.45	2.47
8	3.67	-2.12	17.45	-3.00	3.00
9	2.69	-3.28			

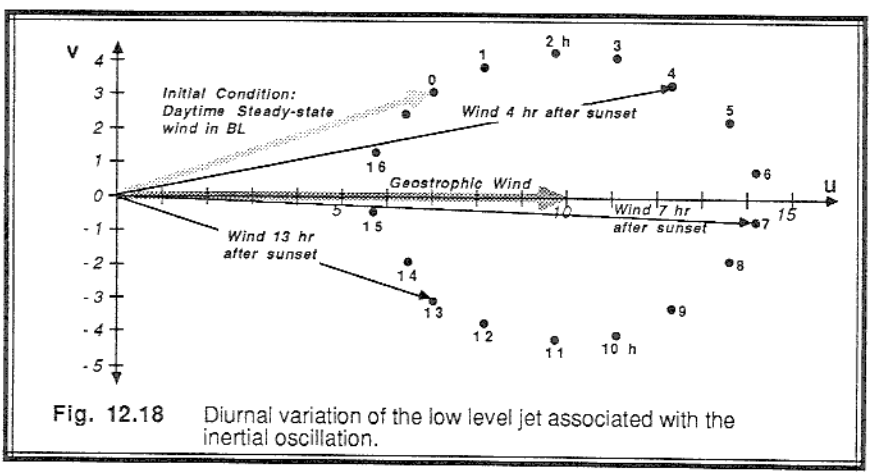

Fig. 12.18 Diurnal variation of the low level jet associated with the inertial oscillation.

12.6 Buoyancy (Gravity) Waves

Statically stable environments support buoyancy waves, so we expect to find waves within the SBL (Gossard and Hooke, 1975). Weakly turbulent SBLs are usually filled with waves. Fig 12.19 shows a sodar record of waves near the Boulder Atmospheric Observatory tower (Hooke and Jones, 1986). This figure clearly exhibits the ubiquitous superposition of waves of various wavelengths and amplitudes.

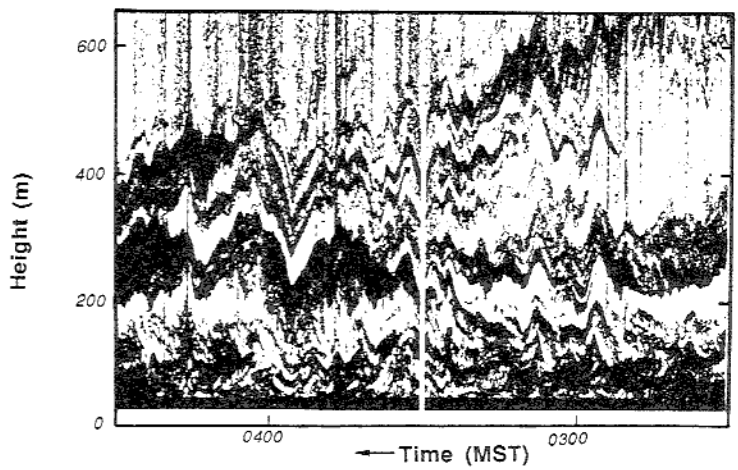

Fig. 12.19 Strata of strong echo returns revealed in a sodar record made at the Boulder Atmospheric Observatory on 11 September 1983. Dark portions of the record denote height-time intervals of strong echo returns that are perhaps turbulent. Gravity waves propagating through the planetary boundary layer perturb these strata and produce the undulations. (After Hooke and Jones, 1986).

12.6.1 Characteristics

Wave frequencies for internal waves at any altitude must be less than the Brunt-Väisälä frequency, N_{BV}, at that height, where:

$$N_{BV}^2 = \frac{g}{\theta_v} \frac{\partial \overline{\theta_v}}{\partial z} \qquad (12.6.1a)$$

Fig 12.20 shows the variation of Brunt-Väisälä frequency as a function of height for the 0300 local time potential temperature sounding plotted in Fig 12.12. Higher stabilities near the surface support a larger range of frequencies than those higher in the SBL. In a residual layer of neutral stratification, vertically propagating waves are not supported, and their amplitude is damped with height within the RL. Waves that propagate upward within the SBL eventually reach a level where their frequency matches the ambient Brunt-Väisälä frequency, at which point they reflect back down toward the ground. Waves are thus trapped between the ground and the neutral layers aloft, resulting in horizontally propagating waves and modal oscillations only, as shown in Figure 12.19. Wave periods (2π/frequency) ranging from less than a minute to 40 min have been reported, depending on the stability. Fig 12.19 shows waves with periods between 1 and 10 minutes.

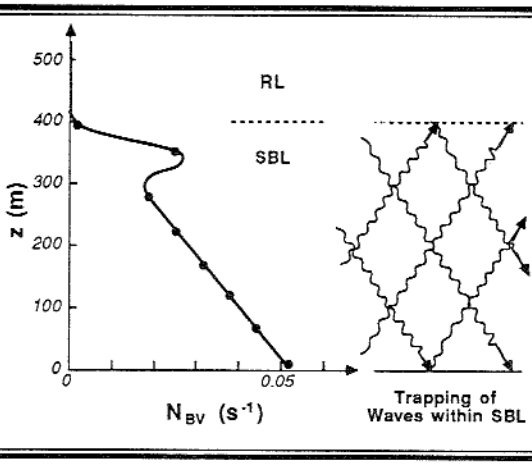

Fig. 12.20 Variation of the Brunt-Väisälä frequency with height for 0300 local time, Night 7, Wangara. Waves are trapped within the SBL.

Vertical wave displacement amplitudes range from fractions of meters to about 200 m (Nai-Ping, et al., 1983; Hooke and Jones, 1986; Finnigan, et al., 1984). Fig 12.19 shows waves with displacement amplitudes between 10 and 100 m. Large amplitude waves can induce surface pressure fluctuations as large as 10 Pa (0.1 mb), although most waves create pressure fluctuations smaller than 5 Pa (0.05 mb). These can be easily measured with surface-based microbarographs. Wave-induced pressure variations can be large compared to the 1 Pa fluctuations associated with typical turbulent wind gusts (Gedzelman, 1983).

Because wave amplitudes can be large compared to the depth of the SBL, we might expect the state of the SBL to be strongly modulated by such waves. This is indeed the case, as is shown for N_{BV}^2, the shear squared, gradient Richardson number, and TKE in Fig 12.21 for one wave period (Finnigan, et al., 1984). For this case, the Richardson

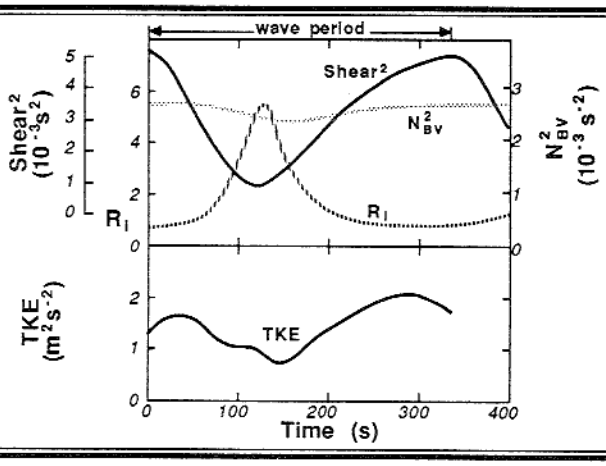

Fig. 12.21 Variation of the shear squared, Brunt-Väisälä squared, Richardson number, and turbulence kinetic energy as a function of wave phase. (After Finnigan, et al., 1984).

number was lowered, dynamic instability induced, and turbulence was generated during portions of the wave cycle, while during other portions turbulence was suppressed. Weinstock (1987) also suggested that some waves can modify the SBL to the point where periods of static instability occur, leading to bursts of convective turbulence during portions of the wave cycle.

Waves can be generated by ***wind shear*** and by ***impulses*** (Gedzelman, 1983). At heights where the Richardson number is small, wind shear can generate K-H waves. These heights are called the ***critical levels***. The K-H waves excite other internal gravity waves that propagate elsewhere in the SBL. Normally, such shear-induced waves have a phase speed equal to the mean wind speed at their critical level. It is possible for multiple critical levels to form, generating a variety of waves that coexist and interact within the SBL. Any shear waves that reflect off the ground back to their respective critical level are absorbed there.

Finnigan, et al. (1984) observed dramatic sequences of large amplitude shear waves at the BAO tower, and computed critical levels at 550 and 650 m for those cases. Hooke and Jones (1986) found that wave-related turbulence can form in thin sheets, perhaps where the Richardson number is small.

Impulse-generated waves have a high coherency, are virtually nondispersive, and are associated with some specific event such as an explosion, thunderstorm, or flow over an obstacle (Gedzelman, 1983). Waves propagate away from this event analogous to water waves propagating away from a pebble thrown into a pond. Often these waves have a long wavelength and large period. As these wave propagate through the SBL, they can induce large displacements of SBL air that modify the shear and stability.

For SBLs that are strongly turbulent, waves are subjected to strong nonlinear interactions with the turbulence. It is an academic question whether such flows should be classified as stably-stratified turbulence, or strongly-nonlinear waves. Any waves generated elsewhere that propagate into the region of strong turbulence will be absorbed by the turbulence, and the wave energy will be converted into TKE.

12.6.2 Analysis Techniques and Governing Equations

We will start with a brief review of linear wave theory, and progress into wave-turbulence interaction. For more details, see Finnigan, et al. (1984), Holton (1972) or Gossard and Hooke (1975).

Linear Wave Theory. Starting with the basic conservation equations described in Chapter 3, we can: (1) expand each dependent variable into a basic state ($\bar{\xi}$, usually assumed as a constant reference background state) and a perturbation wave part (ξ''); (2) assume that the perturbations are small; and (3) eliminate terms consisting of products of perturbation variables because scale analysis shows they are smaller than the other terms.

This process is known as ***linearizing the governing equations***, because the only terms that are left contain basic state variables, or products of the basic state and a single linear perturbation variable. For many special cases, wave solutions can be found

for these equations, resulting in ***linear wave theory***. Some real atmospheric waves appear to have many of the characteristics described by linear wave theory, and are called ***linear waves***. Many others do not, and are sometimes called ***nonlinear waves***.

If κ_x , κ_y and κ_z are the wavenumbers in the x, y, and z directions, respectively, and f is the local wave frequency observed from a fixed point on the ground, then ***linear internal waves*** are described by (Stull, 1976):

$$w'' = A \cdot \sin(J)$$

$$\eta'' = \frac{A}{f_i} \cos(J)$$

$$u'' = -\left(\frac{\kappa_x \kappa_z A}{\kappa_H^2} \right) \sin(J)$$

$$v'' = -\left(\frac{\kappa_y \kappa_z A}{\kappa_H^2} \right) \sin(J)$$

$$p'' = -\left(\frac{\kappa_z \bar{\rho} f_i A}{\kappa_H^2} \right) \sin(J)$$

$$\theta'' = -\left(\frac{A}{f_i} \frac{\partial \bar{\theta}}{\partial z} \right) \cos(J) \qquad (12.6.2a)$$

where the double prime denotes the wave perturbation, and:

η'' is wave vertical displacement,

A is an amplitude parameter,

κ_H is the ***horizontal wavenumber*** defined by $\kappa_H^2 = \kappa_x^2 + \kappa_y^2$,

f_i is the ***intrinsic wave frequency*** defined by $f_i = f - \kappa_x \bar{U} - \kappa_y \bar{V}$, and

$J = \kappa_x x + \kappa_y y + \kappa_z z - f t$.

Also, the following frequency relation must be satisfied:

$$\frac{f_i^2}{N_{BV}^2} = \frac{\kappa_H^2}{\kappa_H^2 + \kappa_z^2} \qquad (12.6.2b)$$

Equations (12.6.2) show that linear waves are deterministic; we can solve for the wave perturbation displacement, vertical velocity, etc. at any location at any time. This is unlike turbulence, where equations (3.5.3) forecast only the statistics of the perturbations. Furthermore, simple sine and cosine functions describe the waves. By looking in time series records for simple sinusoidal oscillations, we can identify linear waves.

Linear waves can transport momentum and kinetic energy vertically, but they can not transport heat or other scalars. For example, (12.6.2a) shows that θ" and w" are 90° out of phase, because one is a sine function and the other is a cosine function. When the product θ"w" is averaged over an integer number of wave periods, the result (i.e., the heat flux) is identically zero.

Nonlinear Waves and Turbulence. Finnigan, et al. (1984) show how analyses of time series data can be extended to include both waves and turbulence. Split any variable, ξ, into three parts: the mean, wave, and turbulence components:

$$\xi = \overline{\xi} + \xi" + \xi' \tag{12.6.2c}$$

The mean is defined by the usual time average (2.4.1a). A phase averaging operator \\ can be defined as:

$$\langle\xi\rangle = \lim_{N\to\infty}\left(\frac{1}{N}\sum_{k=1}^{N}\xi(t + k\,\mathbb{P})\right) \tag{12.6.2d}$$

where $\mathbb{P}$ is the time period of the wave of interest. The wave component can then be found from:

$$\xi" = \langle\xi\rangle - \overline{\xi} \tag{12.6.2e}$$

Knowing both the mean and wave components, these can be subtracted from the instantaneous value to yield the remaining turbulent part from (12.6.2c). The above technique can be used to analyze the wave and turbulence components of an observed time series.

The set of averaging rules for this situation is an extension of the Reynolds averaging rules (Finnigan, et al., 1984):

$$\begin{aligned}
&\langle\xi\rangle = 0 && \overline{\xi"} = 0\\
&\overline{\xi'} = 0 && \overline{\bar{a}\,b} = \bar{a}\,\bar{b}\\
&\langle a"\,b\rangle = a"\langle b\rangle && \langle\bar{a}\,b\rangle = \bar{a}\langle b\rangle\\
&\langle\overline{\xi}\rangle = \overline{\xi} && \overline{\langle\xi\rangle} = \overline{\xi}\\
&\overline{a"b'} = 0 && \overline{\langle a"b\rangle} = 0
\end{aligned} \tag{12.6.2f}$$

Nonlinear waves can transport heat and scalars in addition to energy and momentum. (Hunt, et al., 1985). When (12.6.2c) is used in the basic conservation equations, one can derive averaged conservation equations for turbulence kinetic energy, wave kinetic energy, turbulent heat flux, wave heat flux, etc. using methods analogous to those used in Chapters 2 to 5. A detailed derivation of the averaged equations is beyond the scope of this book. However, the TKE equation for turbulence shown below gives a taste the interaction between waves and turbulence (Finnigan, et al., 1984):

$$\frac{\partial \bar{e}}{\partial t} = \frac{g}{\theta_v}\overline{w'\theta_v'} - \overline{u'w'}\frac{\partial \bar{U}}{\partial z} - \frac{\partial \overline{w'e}}{\partial z} - \frac{1}{\bar{\rho}}\frac{\partial \overline{w'p'}}{\partial z}$$

$$- \overline{r_{ij}''\frac{\partial u_i''}{\partial x_j}} - \overline{u_j''\frac{\partial (r_{ii}''/2)}{\partial x_j}} - \varepsilon \qquad (12.6.2g)$$

where

$$r_{ij}'' = \backslash u_i'u_j' \backslash - \overline{u_i'u_j'} \qquad (12.6.2h)$$

which can be viewed as wavelike fluctuations in the background Reynolds stress due to the presence of the wave. The terms in the first line of (12.6.2g) are the same as those described earlier in (5.1b). The terms in the second line are a result of the wave-turbulence interaction. Also, the viscous dissipation terms are different than those described in Chapter 5.

12.6.3 Spectra

Both waves and turbulence can be present in the SBL. Finnigan, et al. (1984) found that about 20% of the total variance for their case study was explained by coherent wave motion, the remainder being turbulence. The portion of any spectrum composed of idealized linear gravity waves can be identified using cospectral techniques, because vertical motions and temperature will be 90° out of phase. Portions of the spectrum where phase differences are 0 or 180° usually correspond to turbulence. Difficulties can arise because many of the real waves might be highly nonlinear.

For the special case of waves excited at only one wavenumber, we would expect nonlinear interactions to remove the wave energy from the excited wavenumber (***source***) and "spread" it to both higher and lower wavenumbers. The spectrum of a mixture of waves and turbulence can often be split into three subranges (Fig 12.22):

(1) At wavenumbers lower than the source (i.e., large eddies), similarity arguments give a ***-1 power law*** spectral shape [$S(\kappa) \propto \kappa^{-1}$, or $\kappa \cdot S(\kappa) \propto \kappa^{0}$ as in Fig 12.22].

(2) Above the source wavenumber, in the ***buoyancy subrange*** of middle-size eddies, eddies are quasi-two-dimensional because of the suppression of vertical motions by stability. For quasi-2-D turbulence, TKE is not transferred across the spectrum, but ***enstrophy*** (mean-square vorticity) is. Similarity arguments give a ***-3 power law***

spectral shape [$S(\kappa) \propto \kappa^{-3}$, or $\kappa \cdot S(\kappa) \propto \kappa^{-2}$ as in Fig 12.22] for these middle-size eddies.

(3) The inverse of the Ozmidov scale defines the ***buoyancy wavenumber***, which separates the buoyancy subrange (middle wavenumbers) from the inertial subrange (high wavenumbers). At wavenumbers higher than the buoyancy wavenumber, eddies do not feel the static stability directly, are three-dimensional, and obey ***-5/3 power law*** inertial-subrange scaling [$\kappa \cdot S(\kappa) \propto \kappa^{-2/3}$ as in Fig 12.22].

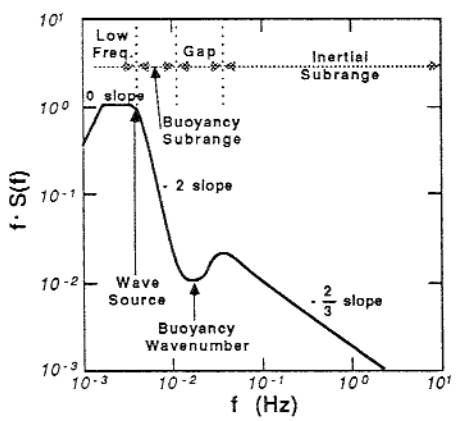

Fig. 12.22
Idealized spectral shape for vertical velocity variance or potential temperature variance for a mixture of waves and turbulence in a SBL. Frequency can be related to wavenumber using Taylor's hypothesis ($f = M \cdot \kappa$). (After Nai-Ping, et al., 1983; and Finnigan et al., 1984).

Within the buoyancy subrange we might expect the only relevant variables to be S, N_{BV}, and κ. Dimensional analysis (Turner, 1973) gives:

$$S(\kappa) \propto N_{BV}^2 \, \kappa^{-3} \qquad (12.6.3)$$

This is the same -3 power law dependence expected using enstrophy arguments.

Between the buoyancy and inertial subranges there is evidence of a gap. This gap is even more apparent in the potential temperature spectrum (Nai-Ping, 1983). One possible explanation (Finnigan, et al., 1984) for the gap is that the energy transfer in the inertial subrange towards lower wavenumbers is blocked at the -3 power law region, leading to a build-up of energy near the buoyancy wavenumber.

Many real atmospheric spectra might be affected by waves at more than one wavelength. The resulting spectrum would be very complex, and would be a function of the relative strengths of the different waves. In addition, Mahrt and Gamage (1987) have found that mesoscale forcings can dominate at low wavenumbers.

12.6.4 Bores

In northern Australia a propagating hydraulic jump phenomenon has frequently been observed during the night and early morning. This undular bore is locally known as the "morning glory", because it is visible on humid mornings as a spectacular-looking, very low-altitude, rapidly propagating (10-15 m/s), rolling, wave-cloud band (Smith, et al., 1982).

A ***bore*** is a rapidly propagating increase in fluid depth, usually associated with tidal signals propagating up estuaries or canals (Lamb, 1932). In the atmosphere, it is believed to be associated with a propagating increase in SBL depth, triggered by a sea breeze or a katabatic flow, and enhanced by the presence of a nocturnal low-level jet (Noonan and Smith, 1986). Bore passage is characterized by a wind squall (surface wind speeds increase from 0.5 m/s to 6 m/s in just a few minutes; wind directions change to point in the direction of bore movement), a pressure increase (0.1 kPa in 10 to 30 min), and the rolling cloud band.

The morning glory phenomenon additionally exhibits a series of 3 to 5 oscillations (of pressure, wind speed, and wind direction) and the corresponding number of cloud bands over a 1 h period at the leading edge of the bore. Because of these oscillations, the phenomenon is classified as an ***undular bore***.

12.7 Terrain Slope and Drainage Winds

12.7.1 Characteristics

Winds formed when cold dense air is accelerated downslope by gravity are called ***drainage winds***, ***gravity flows***, ***slope flows***, or ***katabatic winds***. Brost and Wyngaard (1978) and Mahrt (1981) showed that even gentle slopes of $\Delta z/\Delta x = 0.001$ to 0.01 over a large area can cause drainage winds of 1 to 2 m/s. Slopes at the Wangara field site in Australia were on the order of 0.007, while the average slope of the Great Plains in the USA is roughly 0.001. Both of these sites look flat to the eye, yet slopes are great enough to create drainage winds. Thus, we should expect to have drainage winds just about everywhere within SBLs over land. Kottmeier (1986) observed gravity flows over the Ekström ice shelf.

Large lakes and oceans are about the only places where we can ignore drainage winds. Even the smaller lakes and dry lake beds could be influenced by drainage winds, as cold air from the neighboring slopes drain into the low areas and accumulate as a pool of cold air. Since most weather stations are located in valleys, near rivers, or near lakes, we must expect that the reported winds and temperature are influenced by cold air drainage on radiatively clear nights, and are not representative of the rest of the boundary layer nor of the synoptic flow (assuming light synoptic winds).

Fig 12.23 shows typical profiles of wind in a slope flow. Near the ground, drag reduces the wind speed. Just above the ground where friction is less but the air is still relatively cold, there is a wind maximum or nose. Higher in the profile, shears across the top of the gravity flow in the presence of weaker stability allow significant turbulence,

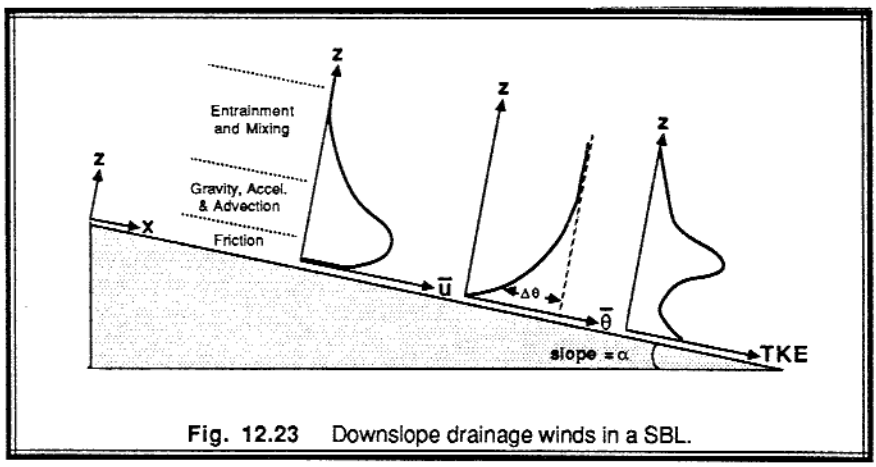

Fig. 12.23 Downslope drainage winds in a SBL.

mixing, and entrainment. Fig 12.23 also shows the typical coordinate system used for modeling studies of slope flows.

As the air flows down the slope, the depth of the drainage flow can grow, and the peak speed can increase. Fig 12.24 shows the slope flow evolution down a 10° average slope covered by grass and short brush (Doran and Horst, 1983; Horst and Doran, 1986). For this case, a very shallow flow with nose at about 50 m over the initial 21° slope evolves into a deeper flow with nose at about 300 m further down the hill where the slope is only 8°.

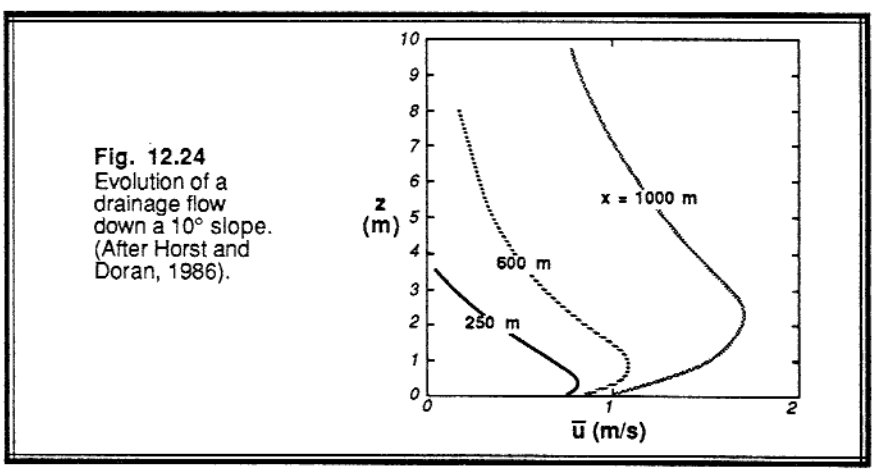

Fig. 12.24 Evolution of a drainage flow down a 10° slope. (After Horst and Doran, 1986).

In the absence of ambient mean flow, drainage wind speeds range between 0.5 to 3.5 m/s. When ambient mean winds are light, the drainage flows in the same direction as the mean wind are enhanced, while those opposing the mean wind are reduced (Yamada,

1983; Heilman and Dobosy, 1985; and Wong, et al., 1987). For moderate and strong mean winds, opposed slope flows are eliminated. Similar interesting interactions between slope flows and sea breezes can occur when mountains are located near the shore. Fitzjarrald (1984, 1986) found that the diurnal cycle of slope flows and land/sea breezes can cause a reversal of the local winds at Veracruz, Mexico.

When drainage winds flow out of a valley into a flatter plain, the leading edge behaves like a weak thunderstorm gust front, with a well-defined nose and K-H waves along the top of the flow. In measurements of such flows past the BAO tower, Blumen (1984) observed the flow to be about 150 m thick, with peak velocities of 4 m/s found below 50 m. The propagation speed of the drainage flow front was estimated to be 2.5 to 3.5 m/s.

12.7.2 Governing Equations

Using the coordinate system shown in Fig 12.23, Mahrt (1982) has written the equation of motion for downslope component of wind as:

$$\underbrace{\frac{\partial U}{\partial t}}_{\text{I}} + \underbrace{U\frac{\partial U}{\partial x}}_{\text{II}} + \underbrace{V\frac{\partial U}{\partial y}}_{\text{III}} + \underbrace{W\frac{\partial U}{\partial z}}_{\text{IV}} = \underbrace{g\frac{\Delta\theta}{\theta}\sin(\alpha)}_{\text{V}} - \underbrace{\cos(\alpha)\frac{g}{\theta}\frac{\partial \bar{\theta}\, h_d}{\partial x}}_{\text{VI}} + \underbrace{f_c V}_{\text{VII}} - \underbrace{\frac{\partial \overline{u'w'}}{\partial z}}_{\text{VIII}} \qquad (12.7.2a)$$

where α is the slope angle, h_d is the depth of the flow, $\Delta\theta(z)$ is the potential temperature difference between the ambient air and the colder slope flow, and the average potential temperature depression in the flow is:

$$\bar{\theta}(z) = \frac{1}{h_d}\int_{z'=z}^{h_d} \Delta\theta \, dz' \qquad (12.7.2b)$$

The terms in the above equation have the following interpretation:

Term I	Acceleration
Term II	Downslope advection
Term III	Cross slope advection
Term IV	Vertical advection
Term V	Buoyancy
Term VI	Thermal wind
Term VII	Coriolis
Term VIII	Stress divergence

Obviously different terms are important for different slopes with different ambient flow conditions. Mahrt (1982) discussed 8 different categories of flow based on a scale

analysis: ***nonstationary, advective-gravity, near equilibrium, shooting, combination, combination with friction, tranquil, and non-gravity***, only two of which will be reviewed here.

For ***advective-gravity flows***, only terms II and V are important. This flow is constant with time, but is a function of downslope distance. The average wind speed over the depth of the flow [using averaging like (12.7.2), except integrated from 0 to h_d] is:

$$\overline{\overline{U}} = \left[\frac{g\,\overline{\overline{\theta}}}{\theta} \cdot x \cdot \sin(\alpha) \right]^{1/2} \tag{12.7.2c}$$

where x is downslope distance. Briggs (1979) suggested a similar equation, but using the surface heat flux instead of the average potential temperature departure:

$$U = 2.15\,[\sin(\alpha)]^{2/9} \left[\frac{g}{\theta} (-\overline{w'\theta'}_s)\, x \right]^{1/3} \tag{12.7.2d}$$

He also suggested that the depth of the flow is given by:

$$h_d = 0.037\,[\sin(\alpha)]^{2/3}\, x \tag{12.7.2e}$$

For ***equilibrium flows***, the pull of gravity is balanced by frictional drag at the top and bottom of the flow (i.e., terms V and VIII are important). These flows are constant in both space and time. The equilibrium average wind speed is:

$$\overline{\overline{U}}_{eg} = \left[\frac{g\,(\overline{\overline{\theta}}/\theta)\,\sin(\alpha)\,h_d}{C_D + C_{Dh}} \right]^{1/2} \tag{12.7.2f}$$

where C_{Dh} is like a drag coefficient, except at the top of the flow: $C_{Dh} = \overline{u'w'}_h / U_{eq}$.

12.7.3 Interactions of SBL Processes

At the start of this chapter, we explored some of the problems associated with SBL modeling. These included factors such as long time scales, turbulence bursting, z-less scaling, inertial oscillations, and now drainage flows. Most of these processes were examined in an idealized scenario in which the other processes were neglected. In the real atmosphere, however, many of these processes can occur simultaneously, making the SBL behavior very difficult to describe.

For example, the accumulated cooling method of examining SBL growth assumes that none of the chilled air is drained away downslope. The downslope flows neglected inertial oscillations. The relationship between fog formation and drainage flow could be

important. Turbulence, mixing, and SBL growth are modulated by buoyancy waves. We conclude that a model of any arbitrary SBL must be designed to include all of the physics described in this chapter in order for it to succeed in all situations. Such a model might be impractical.

12.8 References

Anderson, D.L.T., 1976: The low-level jet as a western boundary current. *Mon. Wea. Rev.*, **104**, 907-921.

Blackadar, A.K., 1957: Boundary layer wind maxima and their significance for the growth of nocturnal inversions. *Bull. Amer. Meteor. Soc.*, **38**, 283-290.

Blumen, W., 1984: An observational study of instability and turbulence in nighttime drainage winds. *Bound.-Layer Meteor.*, **28**, 245-269.

Bonner, W.D., 1968: Climatology of the low level jet. *Mon. Wea. Rev.*, **96**, 833-850.

Briggs, G.A., 1979: Analytic modeling of drainage flows. Draft document, Atmospheric Turbulence and Diffusion Laboratory, NOAA. (Available from EPA, Environmental Sciences Research Lab., Research Triangle Park, NC 27722).

Brook, R.R., 1985: Koorin nocturnal low-level jet. *Bound.-Layer Meteor.*, **32**, 133-154.

Brost, R.A. and J.C. Wyngaard, 1978: A model study of the stably stratified planetary boundary layer. *J. Atmos. Sci.*, **35**, 1427-1440.

Brunt, D., 1939: *Physical and Dynamical Meteorology*, 2nd Ed. Cambridge Univ. Press, Cambridge, GB. 428pp.

Carlson, M.A. and R.B. Stull, 1986: Subsidence in the nocturnal boundary layer. *J. Clim. Appl. Meteor.*, **25**, 1088-1099.

Cerni, T.A. and T.R. Parish, 1984: A radiative model of the stable nocturnal boundary layer with application to the polar night. *J. Clim. Appl. Meteor.*, **23**, 1563-1572.

Chou, M.-D., 1984: Broadband water vapor transmission functions for atmospheric IR flux computations. *J. Atmos. Sci.*, **41**, 1775-1778.

Delage, Y., 1974: A numerical study of the nocturnal atmospheric boundary layer. *Quart. J. Roy. Meteor. Soc.*, **100**, 351-364.

Doran, J.C. and T.W. Horst, 1983: Observations and models of simple nocturnal slope flows. *J. Atmos. Sci.*, **40**, 708-717.

Estournel, C. and D. Guedalia, 1985: Influence of geostrophic wind on atmospheric nocturnal cooling. *J. Atmos. Sci.*, **42**, 2695-2698.

Estournel, C. and D. Guedalia, 1987: A new parameterization of eddy diffusivities for nocturnal boundary layer modeling. *Bound.-Layer Meteor.*, **39**, 191-203.

Estournel, C., R. Vehil and D. Guedalia, 1986: An observational study of radiative and turbulent cooling in the nocturnal boundary layer (ECLATS experiment). *Bound.-Layer Meteor.*, **34**, 55-62.

Finnigan, J.J., F. Einaudi and D. Fua, 1984: The interaction between an internal gravity wave and turbulence in the stably-stratified nocturnal boundary layer. *J. Atmos. Sci.*, **41**, 2409-2436.

Fitzjarrald, D.R., 1984: Katabatic wind in opposing flow. *J. Atmos. Sci.*, **41**, 1143-1158.

Fitzjarrald, D.R., 1986: Slope winds in Veracruz. *J. Clim. Appl. Meteor.*, 25, 133-144.

Garratt, J.R., 1983: Surface influence upon vertical profiles in the nocturnal boundary layer. *Bound.-Layer Meteor.*, **26**, 69-80.

Garratt, J.R., 1985: Inland boundary layer at low latitudes. Part 1, the nocturnal jet. *Bound.-Layer Meteor.*, **32**, 307-327.

Garratt, J.R. and R.A. Brost, 1981: Radiative cooling effects within and above the nocturnal boundary layer. *J. Atmos. Sci.*, **38**, 2730-2746.

Gedzelman, S.D., 1983: Short-period atmospheric gravity waves: a study of their statistical properties and source mechanisms. *Mon. Wea. Rev.*, **111**, 1293-1299.

Godowich, J.M., J.K.S. Ching and J.F. Clark, 1985: Evolution of the nocturnal inversion layer at an urban and non-urban location. *J. Appl. Meteor.*, **24**, 791-804.

Gossard, E.E., J.E. Gaynor, R.J. Zamora, and W.D. Neff, 1985: Fine structure of elevated stable layers observed by sounder and in situ tower measurements. *J. Atmos. Sci.*, **42**, 2156-2169.

Gossard, E.E. and W.H. Hooke, 1975: *Waves in the Atmosphere, Atmospheric Infrasound and Gravity Waves — their Generation and Propagation.* Elsevier Scientific Publ. Co., NY. 456pp.

Hart, J.E., G.V. Rao, H. van de Boogaard, J.A. Young, and J. Findlater, 1978: Aerial observations of the E. African low-level jet stream. *Mon. Wea. Rev.*, **106**, 1714-1724.

Heilman, W. and R. Dobosy, 1985: A nocturnal atmospheric drainage flow simulation investigating the application of one-dimensional modeling and current turbulence schemes. *J. Appl. Meteor.*, **24**, 924-936.

Holton, J.R., 1967: The diurnal boundary layer wind oscillation above sloping terrain. *Tellus*, **19**, 199-205.

Holton, J.R., 1972: *An Introduction to Dynamic Meteorology.* Academic Press, NY. 319pp.

Hooke, W.H. and R.M. Jones, 1986: Dissipative waves excited by gravity wave encounters with the stably stratified planetary boundary layer. *J. Atmos. Sci.*, **43**, 2048-2060.

Horst, T.W. and J.C. Doran, 1986: Nocturnal drainage flow on simple slopes. *Bound.-Layer Meteor.*, **34**, 263-286.

Hunt, J.C.R., J.C. Kaimal and J.E. Gaynor, 1985: Some observations of turbulence structure in stable layers. *Quart. J. Roy. Meteor. Soc.*, **111**, 793-815.

Kottmeier, C., 1986: Shallow gravity flows over the Ekström ice shelf. *Bound.-Layer Meteor.*, **35**, 1-20.

Kraus, H., J. Malcher and E. Schaller, 1985: Nocturnal low-level jet during PUKK. *Bound.-Layer Meteor.*, **31**, 187-195.

Lacser, A. and S.P.S. Arya, 1986: A comparitive assessment of mixing length parameterizations in the stably stratified nocturnal boundary layer (NBL). *Bound.-Layer Meteor.*, **38**, 1-22.

Lamb, H., 1935: *Hydrodynamics* (6th Ed.). Dover, New York. 738pp.

Lettau, H.H., 1967: Small to large scale features of boundary layer structure over mountain slopes. *Proc. Symp. on Mountain Meteor., Colorado State Univ.*, Ft. Collins, Part 2. 1-74.

Mahrt, L., 1981: The early evening boundary layer transition. *Quart. J. Roy. Meteor. Soc.*, **107**, 329-343.

Mahrt, L., 1982: Momentum balance of gravity flows. *J. Atmos. Sci.*, **39**, 2701-2711.

Mahrt, L., 1985: Vertical structure and turbulence in the very stable boundary layer. *J. Atmos. Sci.*, **42**, 2333-2349.

Mahrt, L. and N. Gamage, 1987: Observations of turbulence in stratified flow. *J. Atmos. Sci.*, **44**, 1106-1121.

Mahrt, L. and R.C. Heald, 1979: Comments on "Determining height of the nocturnal boundary layer. *J. Appl. Meteor.*, **36**, 383.

Mahrt, L., R.C. Heald, D.H. Lenschow, B.B. Stankov and IB Troen, 1979: An observational study of the sturcture of the nocturnal boundary layer. *Bound.-Layer Meteor.*, **17**, 247-264.

Malcher, J. and H. Kraus, 1983: Low-level jet phenomena described by an integrated dynamic PBL model. *Bound.-Layer Meteor.*, **27**, 327-343.

Nai-Ping, L., W.D. Neff and J.C. Kaimal, 1983: Wave and turbulence structure in a disturbed nocturnal inversion. *Bound.-Layer Meteor.*, **26**, 141-155.

Nieuwstadt, F.T.M., 1984: The turbulent structure of the stable, nocturnal boundary layer. *J. Atmos. Sci.*, **41**, 2202-2216.

Nieuwstadt, F.T.M., 1984: Some aspects of the turbulent stable boundary layer. *Bound.-Layer Meteor.*, **30**, 31-55.

Noonan, J.A. and R.K. Smith, 1986: Sea-breeze circulations over Cape York Peninsula and the generation of Gulf of Carpentaria cloud line disturbances. *J. Atmos. Sci.*, **43**, 1679-1693.

Raymond, D.J., 1978: Instability of the low-level jet and severe storm formation. *J. Atmos. Sci.*, **35**, 2274-2280.

Sladkovic, R. and H.J. Kantor, 1977: Low-level jet in the Bavarian pre-alpine regime. *Arch. Met. Geoph. Biokl.*, Ser. A., **25**, 343-355.

Smith, R.K., N. Crook and G. Roff, 1982: The Morning Glory: an extraordinary atmospheric undular bore. *Quart. J. Roy. Meteor. Soc.*, **108**, 937-956.

Staley, D.O. and G.M Jurica, 1970: Flux emissivity tables for water vapor carbon dioxide and ozone. *J. Appl. Meteor.*, **9**, 365-372.

Stull, R.B., 1976: Internal gravity waves generated by penetrative convection. *J. Atmos. Sci.*, **33**, 1279-1286.

Stull, R.B., 1983a: Integral scales for the nocturnal boundary layer. Part 1: Empirical depth relationships. *J. Clim. Appl. Meteor.*, **22**, 673-686.

Stull, R.B., 1983b: Integral scales for the nocturnal boundary layer. Part 2: Heat budget, transport and energy implications. *J. Clim. Appl. Meteor.*, **22**, 1932-1941.

Surridge, A.D. and D.J. Swanepoel, 1987: On the evolution of the height and temperature difference across the nocturnal stable boundary layer. *Bound.-Layer Meteor.*, **40**, 87-98.

Turner, J.S., 1973: *Buoyancy Effects in Fluids*. Cambridge Univ. Press, Cambridge, GB. 367pp.

Turton, J.D. and R. Brown, 1987: A comparison of a numerical model of radiation fog with detailed observations. *Quart. J. Roy. Meteor. Soc.*, **113**, 37-54.

Uccellini, L.W. and D.R. Johnson, 1979: The coupling of upper and lower tropospheric jet streams and implications for the development of severe convective storms. *Mon. Wea. Rev.*, **107**, 682-703.

Weinstock, J., 1987: The turbulence field generated by a linear gravity wave. *J. Atmos. Sci.*, **44**, 410-420.

Wong, R.K.W., K.D. Hage and Leslie D. Phillips, 1987: The numerical simulation of drainage winds in a small urban valley under conditions with supercritical Richardson numbers. *J. Clim. Appl. Meteor.*, **26**, 1447-1463.

Wyngaard, J.C., 1973: On surface layer turbulence. *Workshop on Micrometeorology* (Ed. by D. Haugen). Amer. Meteor. Soc., Boston. 101-150.

Xing-Sheng, L., J.E. Gaynor and J.C. Kaimal, 1983: A study of multiple stable layers in the nocturnal lower atmosphere. *Bound.-Layer Meteor.*, **26**, 157-168.

Yamada, T., 1983: Simulations of nocturnal drainage flows by a q^2l turbulence closure model. *J. Atmos. Sci.*, **40**, 91-106.

12.9 Exercises

1) Assume the following PBL initial conditions: time is 1800 local, temperature sounding is adiabatic ($\overline{\theta}$=300 K) up to z = 1 km, above which the lapse rate is $\gamma = \Delta\overline{\theta}/\Delta z$ = 0.01 K/m. Also, assume the following boundary conditions: B = 10 m/K (bulk NBL turbulence parameter), no subsidence, no winds during daytime, and a surface heat flux vs time as plotted below:

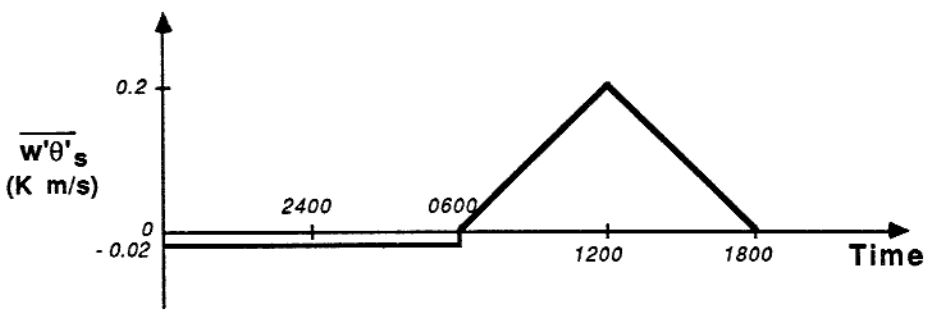

To perform the following exercises, use the thermodynamic (encroachment) method during the day to find the rise of z_i with time, and neglect $\overline{w'\theta'}$ at z_i:

(a) Forecast and plot the depth of the PBL (RL, NBL, and ML) as a function of time for the full 24 h period, starting at 1800 local time on Day 1, and ending at 1800 local time on Day 2.

(b) Also plot the potential temperature profiles at 0600 and 1800 local times for Day 2.

2) What are typical response times of the stable (nocturnal) boundary layer and the mixed layer, and how does the flow vary with these response times?

3) Given: $\langle\overline{\theta}\rangle$ = 5 C at sunset (1800 local time) = constant with height. The following are constant with time during the night:

P_s = 100 kPa (surface pressure)

$\overline{U_g}$ = 5 m/s (geostrophic wind speed)

Z_s = 5000 m (roughness scale)

Q_H = -0.02 K m/s (surface kinematic heat flux)

f_c = 10-4 s-1 (Coriolis parameter)

An orchard owner hires you to forecast the near surface air temperature, because she is concerned about freeze damage to the fruit. Will the near-surface air temperature reach freezing on this night? If so, when? (Hint: Neglect moisture and direct radiative cooling of the trees).

4) Assume a nocturnal boundary layer with Q_H = - 0.02 K m/s (constant throughout the night), Z_s = 3 km. Also assume that the transition to negative heat flux happens at 8 PM local time (call this time t = 0), and that the heat flux becomes positive at 6 AM.

Forecast the depth (h) and strength ($\Delta\overline{\theta}_s$) of the NBL as a function of time for (a) $\overline{U_g}$ = 10 m/s, and (b) $\overline{U_g}$ = 3 m/s.

5) Given the previous answer, plot vertical profiles of $\Delta\overline{\theta}$ corresponding to a local time of 3 AM for both geostrophic-wind cases.

6) Neglecting thermal wind effects, forecast the boundary layer winds in Minneapolis at 3, 6, and 9 h after sunset (assume turbulence ceases at sunset). Given: $\overline{U_g}$ = 8 m/s, $\overline{V_g}$ = 0. Assume that the initial conditions at sunset are $\overline{U}$ = 6 m/s and $\overline{V}$ = 3 m/s. Use the inertial oscillation method to answer this question.

7) Weather stations are often located in the bottom of valleys. Will such a station give surface winds that are representative of the synoptic-scale flow? Why?

8) Name two theories for nocturnal jet formation.

9) Given initial conditions at 1800 local time during Day 1 with an adiabatic temperature profile ($\overline{\theta}$ = 290 K) up to z = z_i = 2 km, no temperature step at the top of the ML, but a constant lapse rate of $\gamma = \partial\overline{\theta}/\partial z$ = 0.01 K/m. Also given the same surface heat flux plotted in question (1), except that the constant nighttime flux is -0.1 K m/s. When in the morning of Day 2 will an elevated thin layer of smoke 500 m above the ground be fumigated down to the ground? Hint: use an exponential-shaped SBL potential temperature profile with B = 10 m/K at night, and use the thermodynamic (encroachment) method for the ML during the day.

10) Calculate the average speed as a function of downslope distance for an advective-gravity flow, where the slope is 20° and the average temperature departure (ambient temperature minus drainage flow temperature) is 3 K.

11) Derive using similarity arguments the spectral power law for enstrophy cascade in a SBL.

12) Prove the averaging rules of (12.6.2f).

13) Derive the linearized equations of motion for which (12.6.2a & b) are solutions.

14) Derive an expression for $\overline{u'w'}$, $\overline{w'\theta'}$ and TKE for a linear wave, using (12.6.2a). Assume the average applies over an integer multiple of wavelengths.